From Gases and Evaporators risk assessmeNt towards an Integrated management of sea and land pollution incidentS

MANIFESTS is a project co-funded by the European Union Civil Protection - DG-ECHO, developed in cooperation with RBINS, CETMAR, IMT Mines Alés, INTECMAR, IST, the UK Security Agency as associated partner and coordinated by CEDRE.

Co-funded by the European Union

Characterisation and detection of a gas cloud

31/03/2026

Work Package	**Gases and Evaporators and risk assessment**
Task	T2.2 Characterisation and detection of a gas cloud
Date	31/03/2026
Version	1
Author/s	Laurent APRIN, Zacaria ESSAIDI (IMT Mines Alès)
Partners	IMT Mines Alès, CEDRE

Co-funded by the European Union

D2.3. Characterisation and detection of a gas cloud
31/03/2026

Co-funded by
the European Union

Table of contents

Tables of illustrations

Co-funded by
the European Union

1. Introduction

The safe handling, transportation, and storage of hazardous liquefied gases — including liquefied natural gas (LNG), liquid ammonia (NH_3), and cryogenic fluids such as liquid nitrogen — represents a growing challenge for the maritime, industrial, and energy sectors. The accidental release of such substances onto water surfaces or into marine environments can generate complex multiphase phenomena involving rapid phase transitions, toxic gas dispersion, significant thermal gradients, and chemical reactions with seawater, all of which pose serious risks to human safety, marine ecosystems, and surrounding infrastructure.

Underwater gas leaks (e.g. pipelines) or release of cryogenic chemical above the water surface can pose significant challenges for responders, as evidenced by the Nord Stream pipeline accident in 2022, or more recently the accident of the Arctic Metagaz ship the 4th of March 2026, carrying LNG from the Arctic port of Murmansk, and attacked by naval drones launched closed to Libyan coast (Figure 1). Such incidents can cause a range of issues, including loss of buoyancy for boats due to the rising of gas, creation of a toxic zone linked to the gas cloud spreading on the water's surface, and risk of fire and explosion. Therefore, it is crucial to assess the timing, location, magnitude, and path of any gas rising to the surface to develop effective response strategies.

Despite the critical importance of understanding these phenomena, experimental data characterizing the physical, chemical, and dispersive behaviour of such releases under realistic conditions remain scarce. Most existing studies focus on idealized or small-scale configurations, and the coupled interactions between subsurface gas dynamics, free-surface hydrodynamics, air-water chemical exchanges, and atmospheric dispersion are rarely captured simultaneously in a single experimental framework.

This report presents the results of a series of medium- to large-scale experimental campaigns aimed at characterizing the behaviour of hazardous gas releases in and above water, conducted at two outdoor facilities: the CEDRE basin and the SDIS 29 training site. Three distinct release scenarios were investigated, each corresponding to a different hazard typology. The first scenario involved the subsurface injection of pressurized methane and ammonia gases into a seawater pool, focusing on the hydrodynamic response of the free surface, the atmospheric dispersion of the released gas, and the chemical impact of ammonia dissolution on the water body. The second scenario characterized the surface release of pressurized liquid ammonia onto a water pool, investigating the coupled thermal, chemical, and dispersive dynamics of the two-phase plume and its interaction with the water surface. The third scenario examined the release of cryogenic liquid nitrogen onto a water surface, with a focus on the rapid vapor cloud propagation, the Leidenfrost effect, and the associated thermal response in both air and water phases.

Together, these three experimental configurations provide a comprehensive and complementary picture of the physical and chemical processes governing hazardous liquid and gas releases onto water surfaces, with direct implications for risk assessment, emergency response planning, and the validation of numerical dispersion models.

Figure 1 : Attack of the Arctic Metagaz ship in Mediterranean Sea the 4th of March 2026

2. Experimental tests Campaigns

2.1. Chemical properties of used chemicals

For this first series of tests, experiments were performed with gaseous pressurized methane and ammonia at ambient temperature. The following paragraphs present information and main useful fluid physical properties of methane and ammonia at equilibrium state (gas and liquid) between 15°C and 30°C. Data are obtained with the WebBook of Chemistry from National Institute of Standards Technology (NIST).

2.1.1. Methane

In the context of the transportation of hazardous materials, LNG is identified with its CAS number and its UN number as follows:

Name	Identification number
CAS number	**8006-14-2** (LNG) / **74-82-8** (Methane)
ONU Number	**1972** (refrigerated fluid) / **1971** (pressurized fluid)

Table 1: LNG identification

The CAS number of a chemical substance, polymer, biological sequence and alloy is its unique registration number in the Chemical Abstracts Service (CAS) database, a division of the American Chemical Society (ACS).

ONU numbers are four-digit numbers that identify hazardous materials in the international transportation of these goods, such as explosive, radioactive, toxic, corrosive, flammable substances, etc.

2.1.1.1. Chemical composition of Methane

Under normal temperature and pressure conditions (i.e. at 25°C and 1.013 bar), LNG is in a gaseous state. LNG consists mainly of methane but also includes up to 10% of ethane and small amounts of other gases (propane and butane in particular).

The composition of LNG varies depending on the deposit from which it comes. The content of the various components respects the following values:

- Methane > 85 % (mol),
- Components C_2 à C_4 < 15 % (mol),
- Sulfur < 0,01 % (masse)

LNG is an odourless, colourless, non-corrosive and non-toxic liquid. In its gaseous phase, LNG can have an anaesthetic effect and/or an asphyxiant effect by reducing the oxygen content of the atmosphere. Contact with the product can cause cold burns.

2.1.1.2. Methane chemical properties

As LNG is a mixture that varies according to the gas field, it is tricky to provide a precise composition and universal physicochemical properties. However, orders of magnitude of the physicochemical properties of LNG can be provided by distinguishing three types of compositions (*Table 2*):

- Pure methane,
- « Light » LNG (methane 97 %),
- « Heavy » LNG (methane 88 %).

Name	Pure methane	"Light" LNG	"Heavy" LNG
Boiling point [°C]	-162	-161	-160
Liquid density at boiling point [kg/m^3]	423	431	464
Vapour density at boiling point [kg/m^3]	1.81	1.80	1.76
Vapour density à 20°C and 1 bar [kg/m^3]	0.67	0.69	0.78
Heat of combustion [MJ/kg]	50	50	49
Flammability range [%]	5-15	4.9-14.9	4.4-14.4
Flash point at atmospheric pressure [°C]	600	-	-
Auto ignition temperature [°C]	-188	-	-
Solubility in water [mg/L]	22	-	-

Table 2: Methane and LNG physicochemical properties [1], [2], [3]

2.1.1.3. Hazard associated to Methane

- **Hazard linked to Methane storage temperature**

As LNG is stored and transported at a temperature of around -160°C, contact between LNG and materials not specifically designed for such low temperatures (known as cryogenic temperatures) can cause them to become fragile and brittle. Furthermore, contact between LNG and the human body can cause cold burns.

- **Hazard linked to the flammability of Methane**

LNG is a flammable liquid, which means that, like petrol or diesel, the vapours it forms can combine with oxygen in the air under certain conditions and give rise to a

combustion reaction. A combustion reaction can give rise to various potentially dangerous phenomena, depending on the exact conditions in which it takes place.

A distinction is thus made between:

- A pool fire, caused by the ignition of LNG vapours created by a pool of LNG released on ground or water. This phenomenon lasts until the LNG is exhausted.

- A cloud fire, caused by the delayed ignition of a drifting cloud of LNG vapours. This phenomenon lasts only a few seconds, with the flame quickly flowing back towards the source of the leak as soon as the contents of the cloud are consumed.

- A "torch" fire, caused by the ignition of a continuous plume of LNG or pressurized natural gas. This phenomenon lasts as long as the leak is fed.

- **Hazard linked to the explosion of an air-gas mixture (vapour cloud explosion)**

The ignition of an LNG vapor cloud or a natural gas plume can create blast waves. In open air, this excess pressure can potentially present a danger to the people, the environment and structures. Potentially dangerous pressure waves (detonation) can potentially appear in confined or congested environments (for example certain complex units in refineries or chemical plants).

- **Hazard linked to the sudden vaporization of Methane released on water**

In the event of a major spill of LNG into the water, a rapid vaporization phenomenon (called "rapid phase transition" or "RPT") can occur, causing overpressure known as a "cold explosion" [1]. This danger exists particularly at the landing stage.

2.1.2. Ammonia

Ammonia is an inorganic chemical compound of nitrogen and hydrogen with the formula NH_3. Ammonia is a colourless gas with a distinctive pungent smell. It is widely used in fertilizers, refrigerants, explosives, cleaning agents, and is a precursor for numerous chemicals [3].

In the context of the transportation of hazardous materials, Ammonia is identified with its CAS number and its UN number as follows:

Name	Identification number
CAS number	**7664-41-7**
ONU Number	**1005**

Table 3: Ammonia identification

2.1.2.1. Ammonia chemical properties

Under normal temperature and pressure conditions (i.e. at 25°C and 1.013 bar), pressurized ammonia is in a gaseous state.

Name	Ammonia
Boiling point [°C]	-33,34
Liquid density at boiling point [kg/m^3]	860
Vapour density at boiling point [kg/m^3]	1.81
Vapour density à 20°C and 1 bar [kg/m^3] [1	0.707
Heat of combustion [MJ/kg]	22.5
Flammability range [%]	15-28
Flash point at atmospheric pressure [°C]	N/A
Auto ignition temperature [°C]	651
Solubility in water [g/L]	895 at 0°C 529 at 20°C

Table 4: Ammonia physicochemical properties [2], [3]

2.1.2.2. Hazard associated to Ammonia

- **Hazard linked to ammonia storage**

The storage of ammonia presents significant risks related to temperature and pressure. Ammonia is generally stored either as a pressurized liquefied gas (approximately 8 to 10 bar at ambient temperature) or as a refrigerated liquid at -33°C at atmospheric pressure. In both cases, a rise in temperature can lead to a dangerous increase in the internal pressure of the tank, potentially resulting in its rupture or even a BLEVE (Boiling Liquid Expanding Vapor Explosion) in the event of a nearby fire. Conversely, refrigerated storage exposes operators to the risk of cryogenic burns in the event of contact with the liquid. In the event of a leak, the rapid vaporization of liquid ammonia is particularly hazardous: one litre of liquid can generate up to 850 litres of gas, instantly forming a toxic and potentially flammable cloud.

- **Health risks**

Ammonia is an irritating and corrosive gas whose health effects vary depending on the concentration and duration of exposure. It can cause irritation of the eyes, nose, throat, and respiratory tract, and at higher concentrations may lead to chemical burns of the lungs and pulmonary oedema. Skin or eye contact can result in severe burns, and at very high concentrations, exposure can be fatal due to asphyxiation or cardiac arrest. Environmentally, ammonia is toxic to aquatic life even at low doses, contributes to the eutrophication of water bodies, and plays a role in the formation of fine particulate matter in the atmosphere. On an industrial level, ammonia is widely used in refrigeration, fertilizer production, and the chemical industry, and any leak can generate a toxic cloud posing a serious risk to surrounding populations. In France, the reference exposure limits established by the INRS set a time-weighted average value (VME) of 20 ppm and a short-term exposure limit (VLE) of 50 ppm.

- **Hazard linked to the flammability and explosion of Ammonia**

From a fire and explosion standpoint, ammonia is flammable within a concentration range of 15 to 28% in air and can explode if ignited in a confined space. Although ammonia is considered only moderately flammable compared to other combustible gases such as propane or methane, it can still create dangerous situations under certain conditions. Its flammability range is relatively narrow, between 15 and 28% concentration in air, and its auto-ignition temperature is quite high, around 630°C, meaning that it requires a significant ignition source to catch fire. However, in the event of a major leak, such as a tank rupture or pipeline failure, ammonia can form a flammable gas cloud. If this cloud encounters an ignition source, it can trigger an explosion, particularly in a confined space where concentrations can quickly reach the explosive range — a phenomenon known as a deflagration. In open spaces, this is referred to as an UVCE (Unconfined Vapor Cloud Explosion). This risk is of particular concern in industrial facilities that use large quantities of ammonia, such as industrial refrigeration systems or fertilizer plants, where a massive leak can generate a gas cloud of sufficient concentration to ignite and cause a significant explosion.

- **Hazard linked to the sudden vaporization of LNG released on water**

While ammonia stored in its refrigerated liquid form at -33°C could theoretically trigger a Rapid Phase Transition (RPT) upon contact with water, this phenomenon should be considered with caution. Unlike liquefied natural gas (LNG), which is stored at much lower temperatures (around -162°C), refrigerated ammonia is significantly less prone to generating the violent explosive vaporization typically associated with RPT events. The temperature differential between liquid ammonia at -33°C and ambient water is considerably smaller than in the case of LNG, which reduces the intensity of the thermal shock and therefore the likelihood of a significant phase transition. That said, a sudden large-scale release of refrigerated liquid ammonia into water cannot be entirely ruled out as a potential source of rapid vaporization, particularly if the release is massive and

the contact is instantaneous. In such a scenario, the primary concern would remain the rapid formation of a toxic ammonia gas cloud rather than a significant mechanical shock wave.

2.2. Large test scale of underwater gas release

2.2.1. Methane experiments

The test campaign carried out in July 2025 was conducted in the CEDRE's basin (Figure 2). Four different flow rates were tested por methane (100 L/min, 200 L/min, 300 L/min, and 400 L/min) and three flow rates were tested for ammonia (100 L/min, 200 L/min 300 L/min) over a duration between 1 and 2 minutes.

For ammonia tests, two explosimeters were located vertically above the release and the other 3 m away from the release (Figure 3). All experimental sensors and equipment used for these tests are listed Table 5.

Name	Supplier	Acquisition data rate / measurement range
Datalogger	National Instrument	0.1 s
Thermocouple T	TC-SA	-200°C – 400°C
Pressure sensors	Omega	0 -10 bar
Water pH and Temperature	NKE Instrumentation WiMo	2s
Mass flow regulator	BROOKS SLA5853	1 s
Water current sensor	VECTOR 3D acoustic velocimeter	0.1 s
Explosimeter	Draeger 6811525	15 s

Table 5: List of experimental devices and sensors used for ammonia tests performed in July 2025 (basin trial)

Figure 2: Illustration of the CEDRE experimental device used for basin tests performed in July 2025

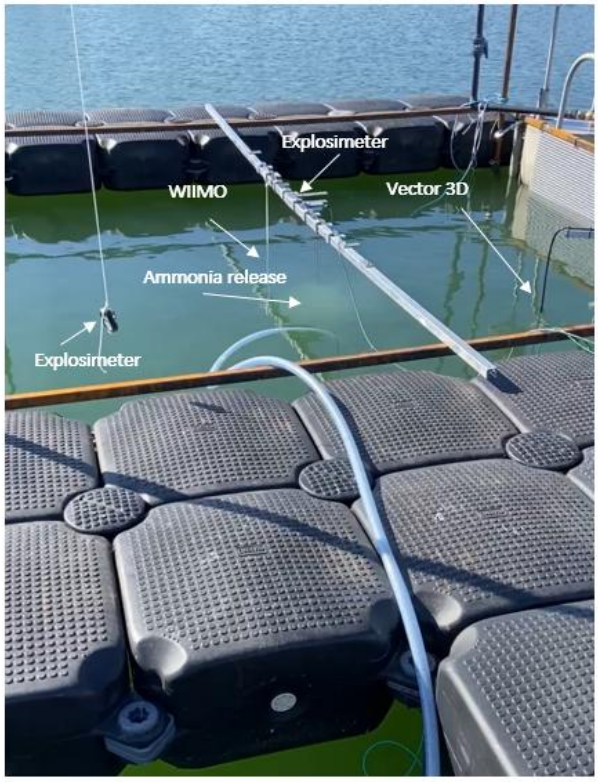

Figure 3: Location of the experimental devices used during ammonia basin test in July 2025

2.2.2. Methane results

2.2.2.1. Experimental setup

The experimental setup is shown schematically in Figure 4. It consists of a metallic framework fabricated from square-section steel tubes. The tubes were assembled into a freestanding structure with a square base of side length 4 m and an overall height of 5 m (Figure 4). The gases under investigation were supplied through a feed pipe and discharged via a circular nozzle positioned at the center of the square base, located at the bottom of a seawater pool (2.5m under the water surface). The nozzle had an inner diameter of approximately $d_{inner} = 7{,}8\ mm$.

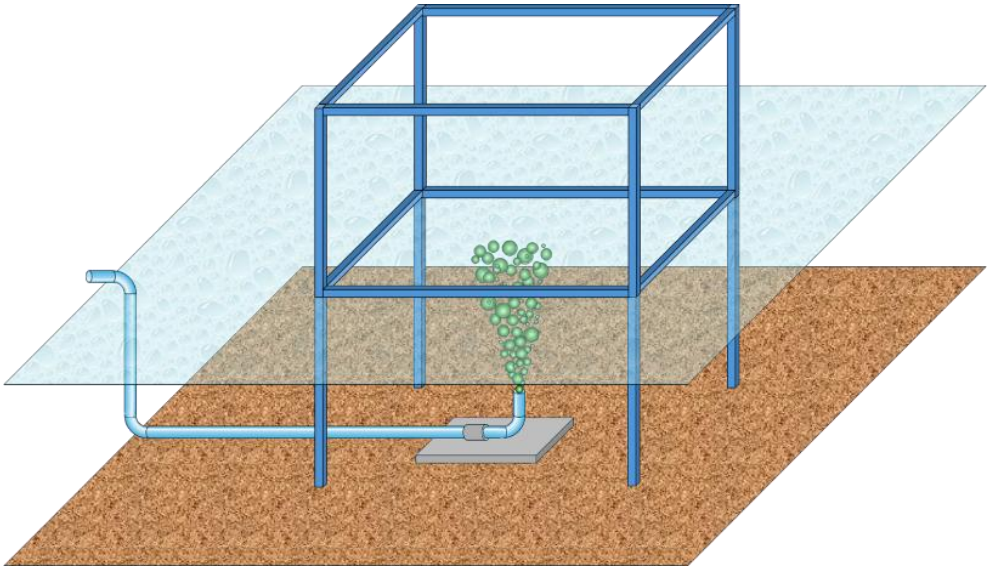

Figure 4: Schematics for the gas release through a circular nozzle in the bottom of seawater pool

Figure 5 presents pictures of the complete experimental apparatus corresponding to the schematics introduced previously. The metallic supporting frame is shown in the right-hand image. A water-curtain device was installed along one of the upper horizontal metal bars, on the right side of the frame. To quantify the spatial variability of the basin free surface, a square grid with 2 cm spacing was positioned in the background of the Canon 5D Mark III field of view.

Figure 5: Preparation of the experimental setup for the gas release in the bottom of seawater pool

The investigated gases were supplied from 50 L pressurized cylinders (left-hand image). The volumetric flow rate was regulated using a calibrated BROOKS SL5853S volumetric flow controller, after which the gas was conveyed via tubing to a nozzle placed at the bottom of the basin. Gas pressure and temperature were measured in the vicinity of the nozzle.

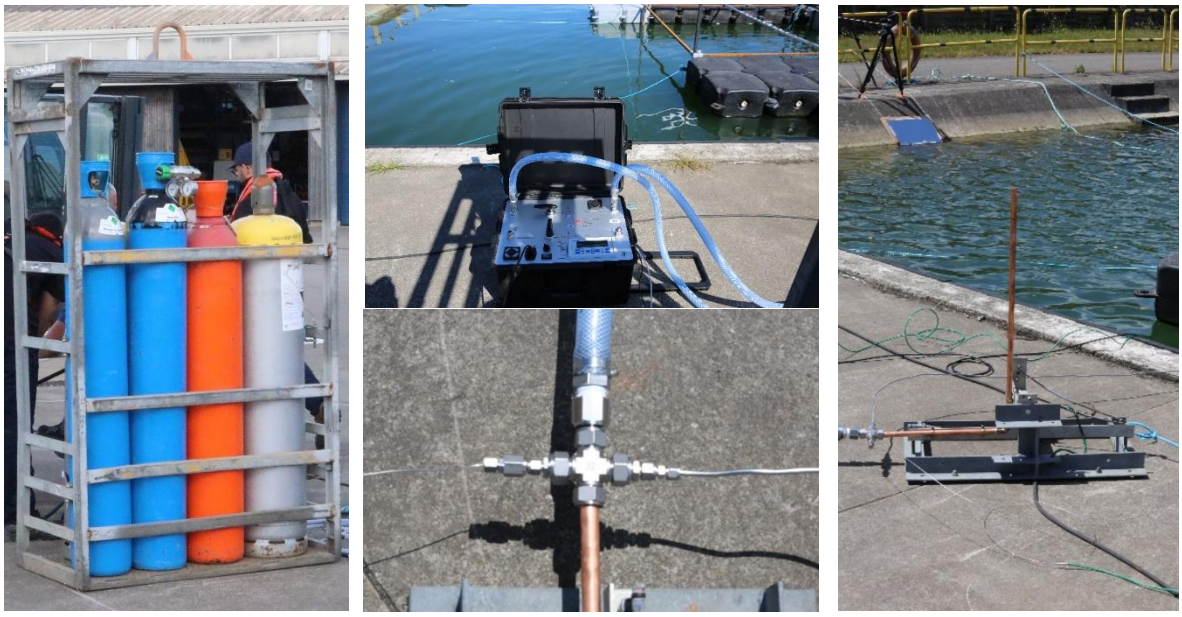

Figure 6: Preparation of the experimental setup for the gas release in the bottom of the seawater pool (50 l industrial gas cylinder, Flowmeter regulator, Temperature and pressure sensors, Nozzle)

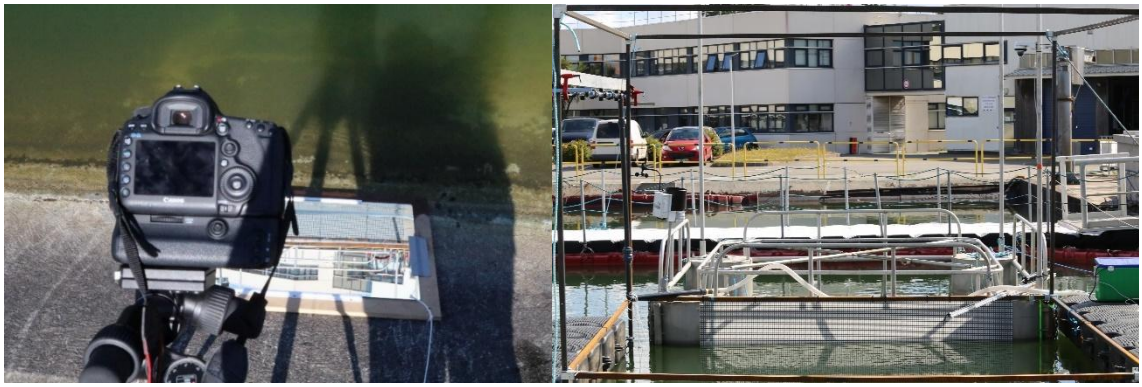

Figure 7 : Visualization of the gas flow released in the bottom of seawater pool with a Canon 5D Mark III camera equipped with a Canon EF 70 – 200 mm f/2.8L USM canon objective (left image), and high-resolution dome surveillance camera (top of the right image)

A Canon 5D Mark III camera equipped with a Canon EF 70-200 mm, f/2.8L USM canon objective was employed to investigate the free surface elevation when the methane is released. This camera is equipped with a CMOS sensor featuring a resolution of 5760×3840 pixels, with square pixels of 6.5µm size, allowing the image resolution to be adjusted according to experimental requirements. In the present study, the full sensor resolution was used for image acquisition, while video recordings of the methane gas release were performed at a resolution of 1920 x 1080 pixels with an acquisition rate of 25 frames per second (Figure 7).

Figure 8 shows typical images cropped images obtained with the Canon 5D Mark III Camera with and without free surface elevation of the seawater pool resulting from the methane gas release a flow rate $Q_v = 100\ l/min$.

972A2545_000001 # 972A2545_000999

Figure 8 : Example of seawater free surface elevation observed during a methane gas release in the bottom of seawater pool (video 972A2545 - Flow rate CH_4 $Q_v = 100\ l/min$)

2.2.2.2. Water level elevation

In order to visualize and quantify the spatial displacements of the seawater free surface induced by methane gas release into the pool, a high-contrast black-and-white grid was

positioned behind the region of interest at the gas outlet. The grid comprised square cells with a side length of 2 cm (vertical and horizontal lines). Free-surface deformations were recorded from the front using a Canon EOS 5D Mark III camera equipped with a Canon EF 70-200 mm f/2.8L USM lens; the field of view was adjusted to circumscribe the measurement region.

Video recordings of the free-surface elevation during methane injection were processed in MATLAB using custom image-processing routines developed to extract quantitative descriptors of the free-surface profile. For each imposed flow rate Q_v, the corresponding video was decomposed into individual frames. The RGB frames were cropped to the area of interest and converted to grayscale, with subsequent intensity adjustment to enhance contrast. Spatial gradient images were then computed to maximize the distinction between the background grid and the free-surface boundary. Segmentation steps were applied to separate the background pattern from the free-surface region. The resulting images were subsequently binarized and subjected to morphological cleaning to obtain a continuous free-surface contour. A simplified diagram of the processing procedure is provided in Figure 9.

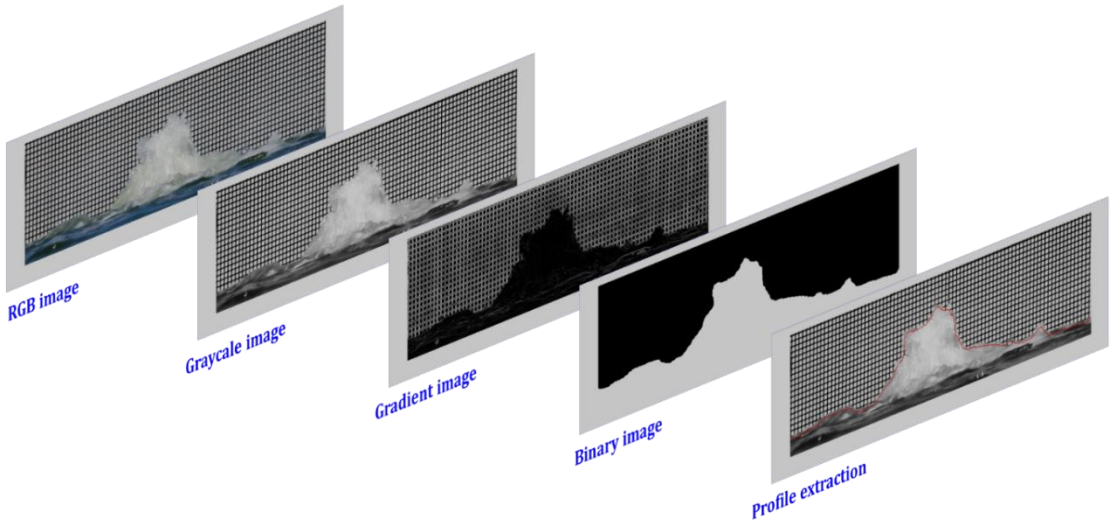

Figure 9: Image processing procedure for the extraction of the seawater free surface profile (from left to right: RGB frame is circumcised to the area of interest and converted to grayscale representation. Spatial intensity gradients were then computed to localize the free surface boundary, then, the images are binarized to isolate the free surface profile as illustrated by the red curve in the final image.)

For each flow-rate condition, the extracted free-surface profiles from all frames were assembled into a temporal representation to visualize the progressive evolution of the free surface. The spatiotemporal variations obtained for four methane flow rates: Q_{V1}=100 L/min, Q_{V2}=200 L/min, Q_{V3}=300 L/min and Q_{V4}=400 L/min are reported in Figure 7.

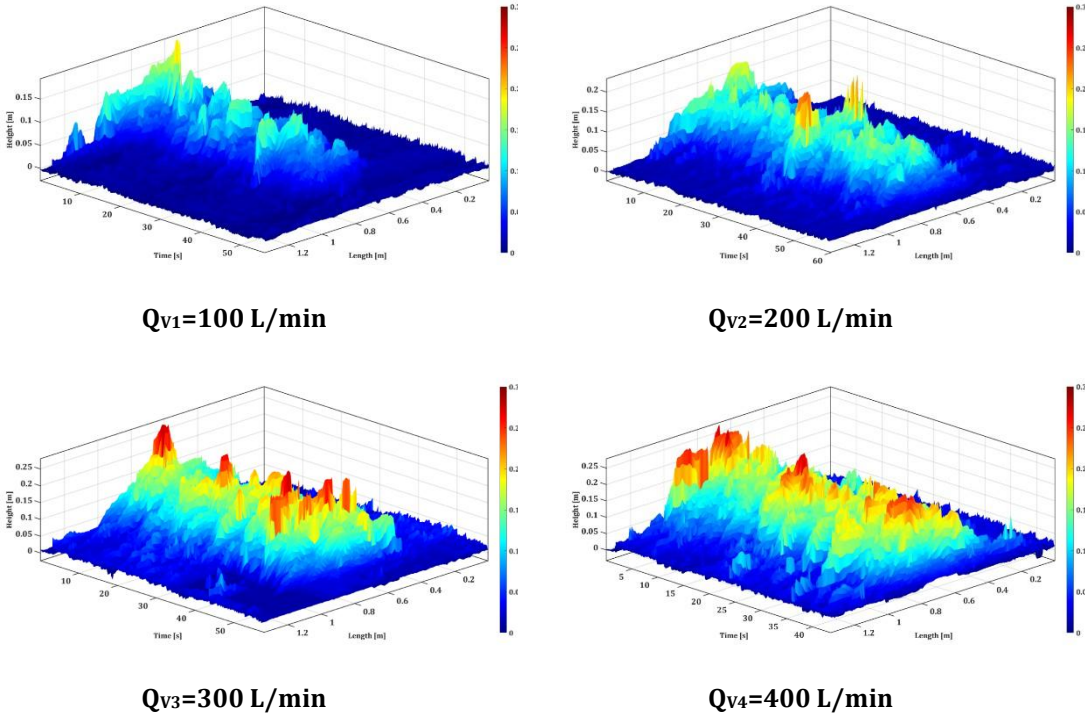

Q_{V1}=100 L/min **Q_{V2}=200 L/min**

Q_{V3}=300 L/min **Q_{V4}=400 L/min**

Figure 10: Temporal variations of the seawater pool free surface changes observed during the release of methane gas with 4 flow rates ($Q_{v1} = 100\ l.min^{-1}$, $Q_{v2} = 200\ l.min^{-1}$, $Q_{v3} = 300\ l.min^{-1}$ and $Q_{v4} = 400\ l.min^{-1}$)

For comparative purposes, an identical spatial scale was applied to all reconstructions, as indicated by the colour bar fixed at 0.3 m. The three-dimensional visualizations employ a colour-coded elevation scale spanning 0 m to 0.3 m representing the free-surface elevation, h. Dark blue regions correspond to an undisturbed, planar water surface (h=0 m), observed both prior to and following the release of methane gas, whereas dark red denotes the maximum elevation (h=0.3 m). Intermediate elevations are represented by intermediate colours on the same scale.

The results demonstrate a monotonic increase in free-surface elevation h with increasing gas flow rate Q_v. To obtain quantitative descriptors of this response, the median elevation profile associated with each flow condition was fitted using two Gaussian models. The first model (Gaussian A) constrains the baseline offset to zero, while the second model (Gaussian B) permits a variable baseline. Comparing these formulations enables identification of the most appropriate model and the best-fitting representation of the measured profiles.

2.2.2.3. General model Gaussian A:

The one-dimensional Gaussian function used for the first approximation of the median free surface water elevation is defined by equation (1):

$$f_1(x) = a_1 * exp\left(-\frac{(x-b_1)}{c_1}\right)^2 \quad (1)$$

where $a_1$denotes the amplitude, $b_1$the centroid (location parameter), and c_1a scale parameter related to the peak width.

The parameters a_1, b_1, and c_1 were determined for four controlled methane gas release experiments conducted at nominal volumetric flow rates. The resulting values are summarized in Table 6.

Coefficients [m]	$100\ [l/min]$	$200\ [l/min]$	$300\ [l/min]$	$400\ [l/min]$
a_1	0.0407	0.06053	0.07818	0.09511
b_1	0.6766	0.7056	0.693	0.6919
c_1	0.1735	0.2552	0.315	0.3085

Table 6: Summary of the gaussian parameters (equation 1) obtained for the 4 releases of methane gas with 4 flow rates ($Q_{v1} = 100\ l.min^{-1}$, $Q_{v2} = 200\ l.min^{-1}$, $Q_{v3} = 300\ l.min^{-1}$ and $Q_{v4} = 400\ l.min^{-1}$)

Figure 11 presents the variation of the fitted model parameters as a function of the methane gas release volumetric flow rate. Several trends emerge from these data. First, the parameter a_1, associated with the elevation h of the no disturbed seawater free surface, increases linearly over the investigated range [$100\ l.min^{-1} - 400\ l.min^{-1}$]. Second, the parameter b_1, which represents the spatial location (centroid) of the Gaussian distribution, remains nearly invariant, indicating that the median position of the modelled Gaussian is insensitive to changes in gas release flow rate within the studied conditions. Third, the parameter c_1, corresponding to the Gaussian width, increases with increasing methane flow rate and subsequently approaches a plateau, with saturation observed for $Q_{v3} = 300\ l.min^{-1}$.

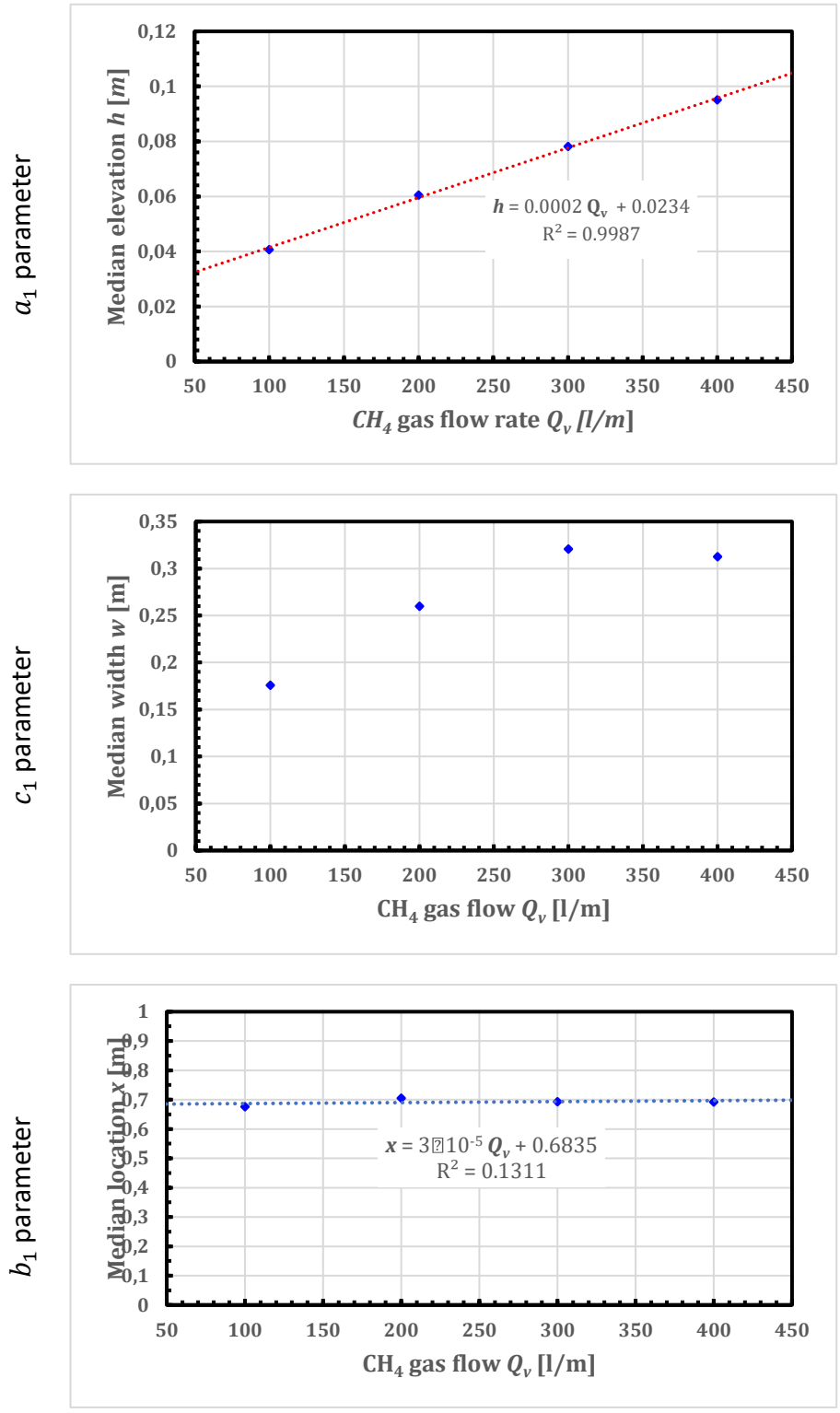

Figure 11 : Variations of the modelled gaussians parameters (a_1, b_1 and , c_1) for the seawater pool free surface changes observed during the release of methane gas with 4 flow rates ($Q_{v1} = 100\ l.min^{-1}$, $Q_{v2} = 200\ l.min^{-1}$, $Q_{v3} = 300\ l.min^{-1}$ and $Q_{v4} = 400\ l.min^{-1}$)

Co-funded by
the European Union

The 95% confidence intervals associated with each parameter are reported in Table 2. The standard deviation associated with the free surface elevation profile for each methane gas release flow rate is illustrated by a transparent grey envelope surrounding the median free surface profile in Figure 12. These results indicate pronounced variability in the free-surface seawater elevation near the crest (i.e., upper portion) of the Gaussian profile.

Coefficients [m]	$100\ [l/min]$	$200\ [l/min]$	$300\ [l/min]$	$400\ [l/min]$
a_1	[0.04022, 0.04117]	[0.0596, 0.06146]	[0.07701, 0.07935]	[0.09407, 0.09616]
b_1	[0.675, 0.6783]	[0.7024, 0.7088]	[0.6891, 0.6968]	[0.6891, 0.6946]
c_1	[0.1712, 0.1758]	[0.2507, 0.2597]	[0.3096, 0.3205]	[0.3046, 0.3124]

Table 7: Summary of the 95% confident bounds related to the gaussian parameters (equation E_1) obtained for the release of methane gas with four flow rates ($Q_{v1} = 100\ l.min^{-1}$, $Q_{v2} = 200\ l.min^{-1}$, $Q_{v3} = 300\ l.min^{-1}$ and $Q_{v4} = 400\ l.min^{-1}$)

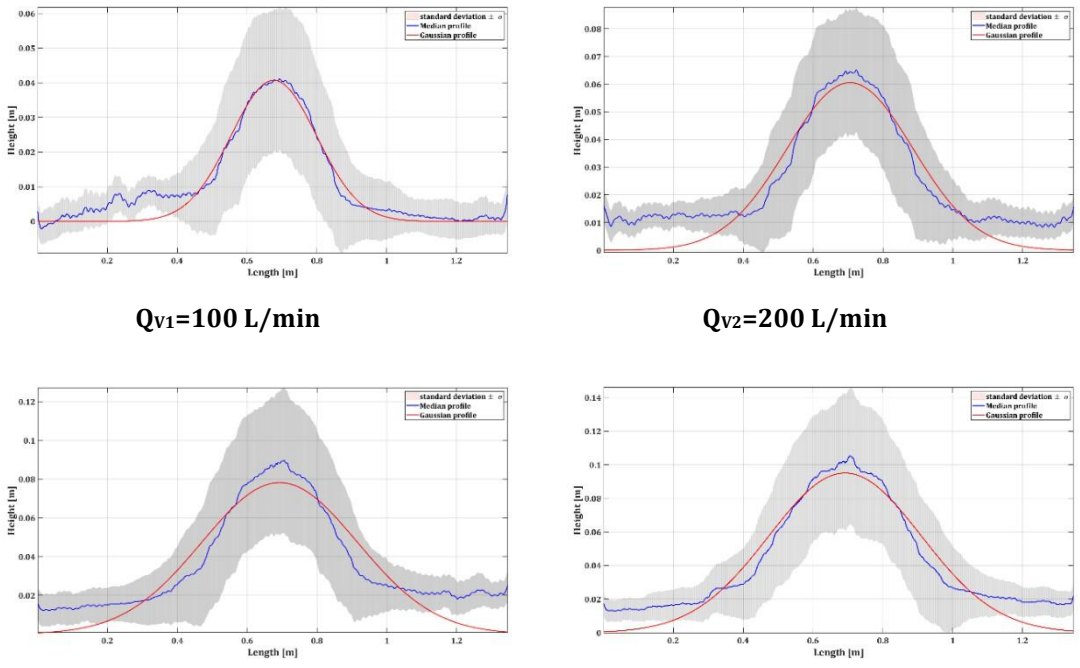

Q_{V1}=100 L/min **Q_{V2}=200 L/min**

Q_{V3}=300 L/min **Q_{V4}=400 L/min**

Figure 12 : Gaussian fits (equation E_1) for the median profile of the temporal variations of the seawater pool free surface changes observed during the release of methane gas with four flow rates ($Q_{v1} = 100\ l.min^{-1}$, $Q_{v2} = 200\ l.min^{-1}$, $Q_{v3} = 300\ l.min^{-1}$ and $Q_{v4} = 400\ l.min^{-1}$). The baseline is fixed to $0\ m$

Co-funded by the European Union

The Gaussian approximation defined by equation (1) exhibits divergence near the domain tails as one moves away from the center of the jet and fails to accurately reproduce the median seawater elevation, with the discrepancy becoming more pronounced as the methane gas flow rate increases. These limitations indicate that an alternative modelling approach is required to provide a more faithful representation of the observed elevation profile.

2.2.2.4. General model Gaussian B:

In order to improve the theoretical agreement with the median free-surface elevation profile, the original model (equation (1)) was revised to account for baseline variations. Accordingly, a one-dimensional Gaussian approximation with an explicit baseline term was adopted, yielding the following expression:

$$\boldsymbol{f_2(x) = a_2 * exp\left(-\frac{(x-b_2)}{c_2}\right)^2 + d_2} \quad (2)$$

where $\boldsymbol{a_2}$ denotes the amplitude, $\boldsymbol{b_2}$ the centroid (location), $\boldsymbol{c_2}$ a parameter related to the peak width, and $\boldsymbol{d_2}$ the baseline offset.

The parameters (a_2, b_2, c_2 and , d_2) were estimated for methane releases conducted at four volumetric flow rates: $Q_{v1} = 100\ l.min^{-1}$, $Q_{v2} = 200\ l.min^{-1}$, $Q_{v3} = 300\ l.min^{-1}$ and $Q_{v4} = 400\ l.min^{-1}$. The resulting parameter values are summarized in Table 3.

Coefficients [m]	**100 $[l/min]$**	**200 $[l/min]$**	**300 $[l/min]$**	**400 $[l/min]$**
$\boldsymbol{a_2}$	0.03911	0.05517	0.07173	0.08669
$\boldsymbol{b_2}$	0.6781	0.706	0.6882	0.6914
$\boldsymbol{c_2}$	0.1548	0.1812	-0.1963	-0.2229
$\boldsymbol{d_2}$	0.002734	0.0109	0.01737	0.01651

Table 8: Summary of the gaussian parameters (equation(2)) obtained for the 4 releases of methane gas with 4 flow rates ($Q_{v1} = 100\ l.min^{-1}$, $Q_{v2} = 200\ l.min^{-1}$, $Q_{v3} = 300\ l.min^{-1}$ and $Q_{v4} = 400\ l.min^{-1}$)

Figure 13 shows the dependence of the fitted parameters a_2, b_2, c_2, and d_2 on the methane volumetric flow rate, Q_v. Parameter estimation based on equation (2) provides an improved representation of the median free-surface seawater elevation profile. The resulting trends are consistent with those reported previously (Figure 11). Specifically,

the free-surface elevation amplitude a_2 increases linearly with Q_v, exhibiting characteristics comparable to a_1 over the range $[100\ l.min^{-1} - 400\ l.min^{-1}]$. The Gaussian centroid location, quantified by b_2, remains approximately constant, indicating that the modelled Gaussian peak does not shift appreciably with increasing volumetric flow rate Q_v. In contrast, the Gaussian width parameter c_2 exhibits a linear increase in magnitude (i.e., $|c_2|$ increases) as Q_v increases. Finally, the plateau behaviour previously observed for c_1 is instead manifested in the baseline free-surface elevation parameter d_2.

All parameters (a_2, b_2, c_2, and d_2) were obtained from methane release experiments conducted at four flow rates: $Q_{v1} = 100\ l.min^{-1}$, $Q_{v2} = 200\ l.min^{-1}$, $Q_{v3} = 300\ l.min^{-1}$ and $Q_{v4} = 300\ l.min^{-1}$.

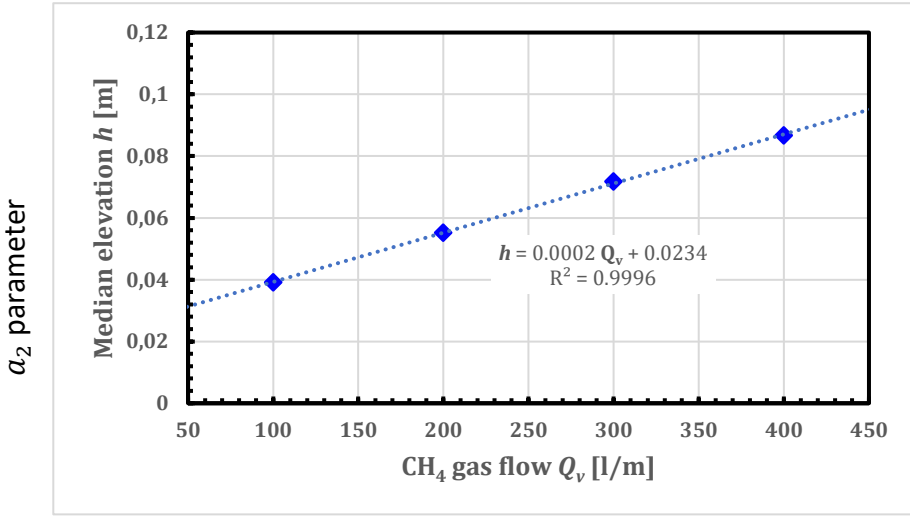

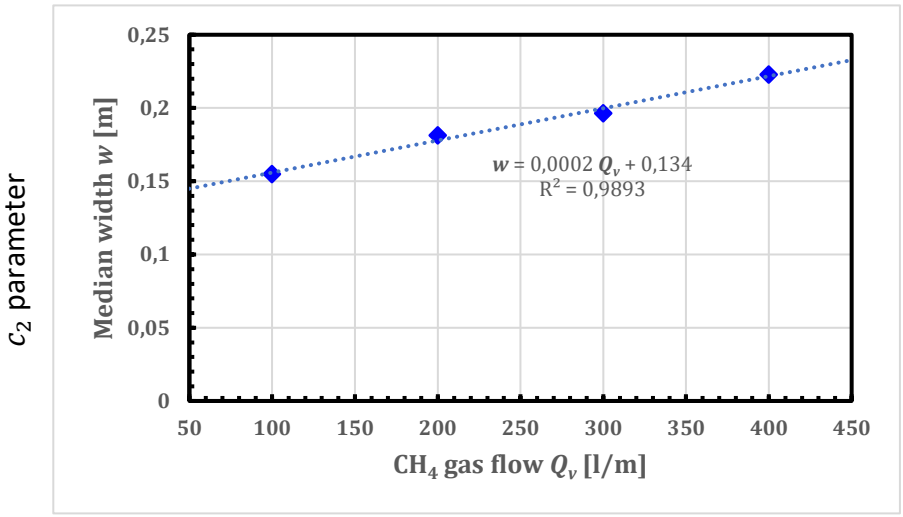

Co-funded by
the European Union

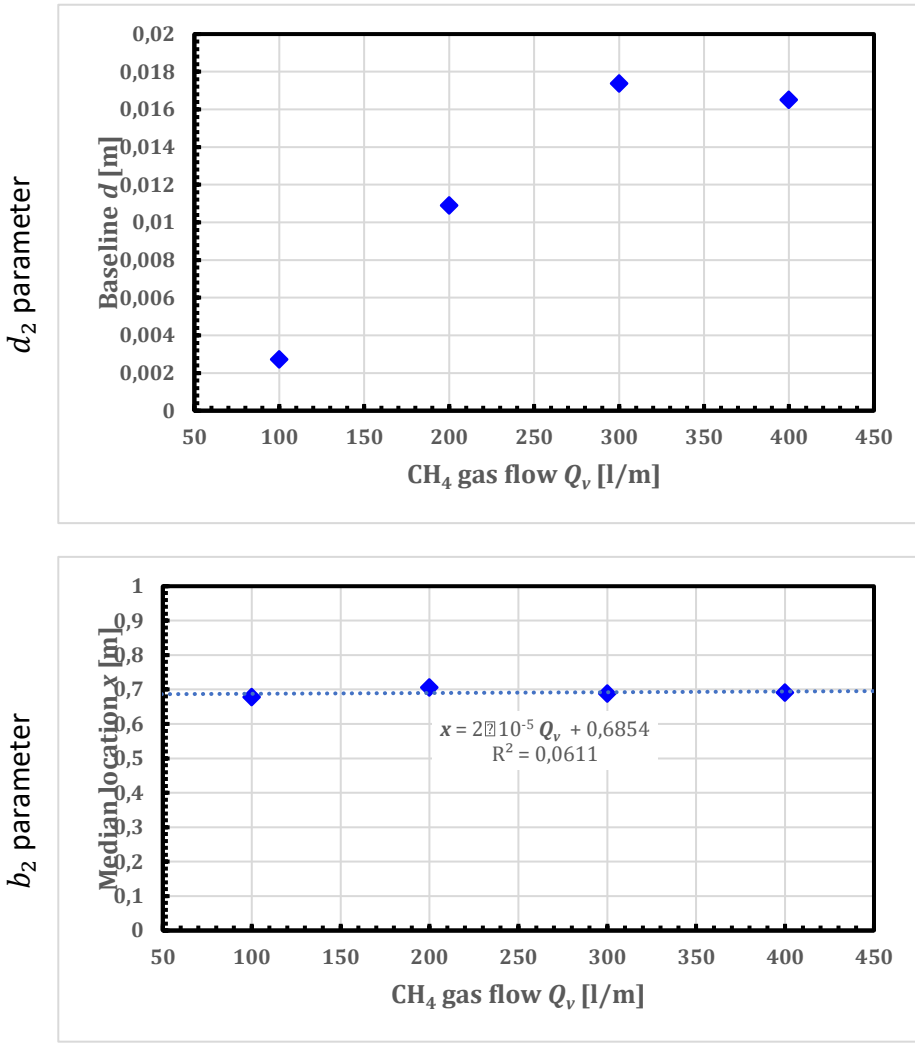

Figure 13: Variations of the modelled gaussians parameters (a_2, b_2, c_2 and , d_2) for the seawater pool free surface changes observed during the release of methane gas with 4 flow rates ($Q_{v1} = 100\ l.min^{-1}$, $Q_{v2} = 200\ l.min^{-1}$, $Q_{v3} = 300\ l.min^{-1}$ and $Q_{v4} = 300\ l.min^{-1}$)

Table 9 reports the 95% confidence intervals for each estimated parameter. The standard deviation associated with the free surface elevation profile for each CH_4 gas release flow rate is depicted by a transparent gray envelope surrounding the median free surface profile in Figure 14. As shown in Figure 12, the theoretical Gaussian model exhibits improved agreement with the median free-surface seawater elevation profile.

Coefficients [m]	100 $[l/min]$	200 $[l/min]$	300 $[l/min]$	400 $[l/min]$
a_2	[0.03872, 0.0395]	[0.05491, 0.05542]	[0.07131, 0.07215]	[0.08635, 0.08703]
b_2	[0.6769, 0.6793]	[0.7054, 0.7067]	[0.6873, 0.6891]	[0.6908, 0.6921]
c_2	[0.1529, 0.1567]	[0.1802, 0.1823]	[-0.1978, -0.1948]	[-0.2241, -0.2218]
d_2	[0.002579, 0.002888]	[0.01079, 0.01102]	[0.01716, 0.01757]	[0.01632, 0.0167]

Table 9: Summary of the gaussian parameters (equation (2)) obtained for the 4 releases of methane gas with 4 flow rates ($Q_{v1} = 100\,l.min^{-1}$, $Q_{v2} = 200\,l.min^{-1}$, $Q_{v3} = 300\,l.min^{-1}$ and $Q_{v4} = 400\,l.min^{-1}$)

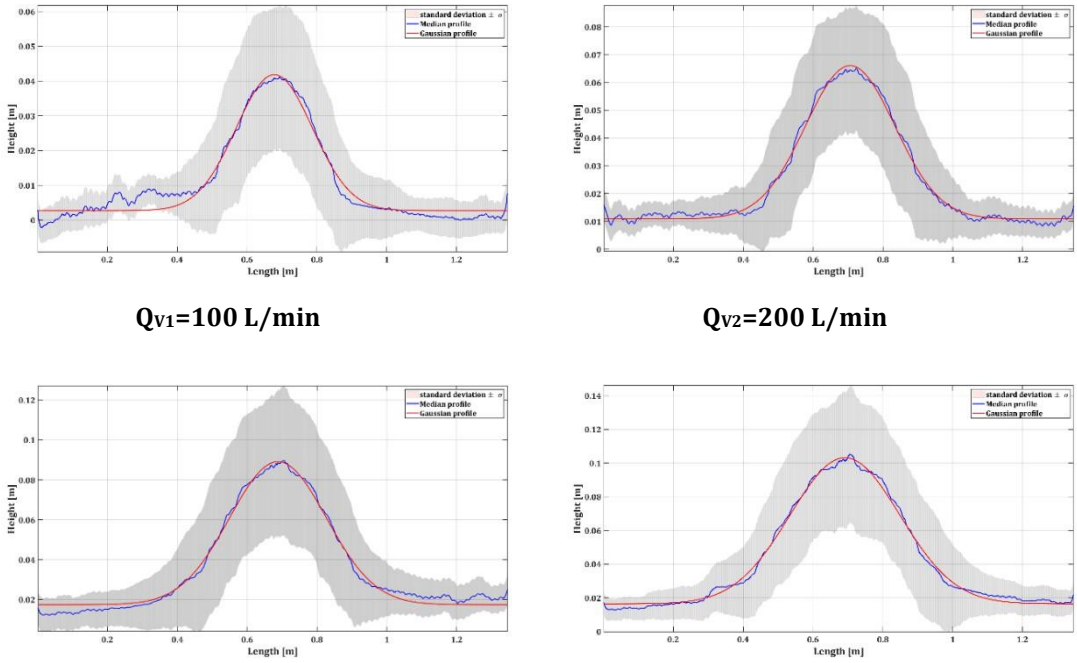

Q_{V1}=100 L/min **Q_{V2}=200 L/min**

Q_{V3}=300 L/min **Q_{V4}=400 L/min**

Figure 14: Gaussian fits (equation (2)) for the median profile of the temporal variations of the seawater pool free surface changes observed during the release of methane gas with 4 flow rates ($Q_{v1} = 100\,l.min^{-1}$, $Q_{v2} = 200\,l.min^{-1}$, $Q_{v3} = 300\,l.min^{-1}$ and $Q_{v4} = 400\,l.min^{-1}$). The baseline is variable to achieve the best gaussian fit

Figure 15 shows the maximum water surface elevation measured during experimental trials conducted to simulate a subsea methane pipeline leak. The results demonstrate a clear and consistent linear relationship between the gas flow rate and the maximum surface elevation, described by the following equation:

$$\boldsymbol{h = 0.0002\, Q_v + 0.0234} \quad (3)$$

where *h* is the maximum elevation in meters and Q_v is the gas flow rate in L/min. The excellent coefficient of determination (R^2 = 0.9996) confirms that this linear model fits the experimental data almost perfectly, indicating a highly predictable and stable hydraulic behaviour within the tested flow rate range. At 100 l/min, the maximum surface elevation was approximately 4.2 cm, rising to around 10.5 cm at 400 l/min. While these elevations may appear moderate, they are accompanied by significant transverse currents and surface turbulence generated by the rising gas bubbles.

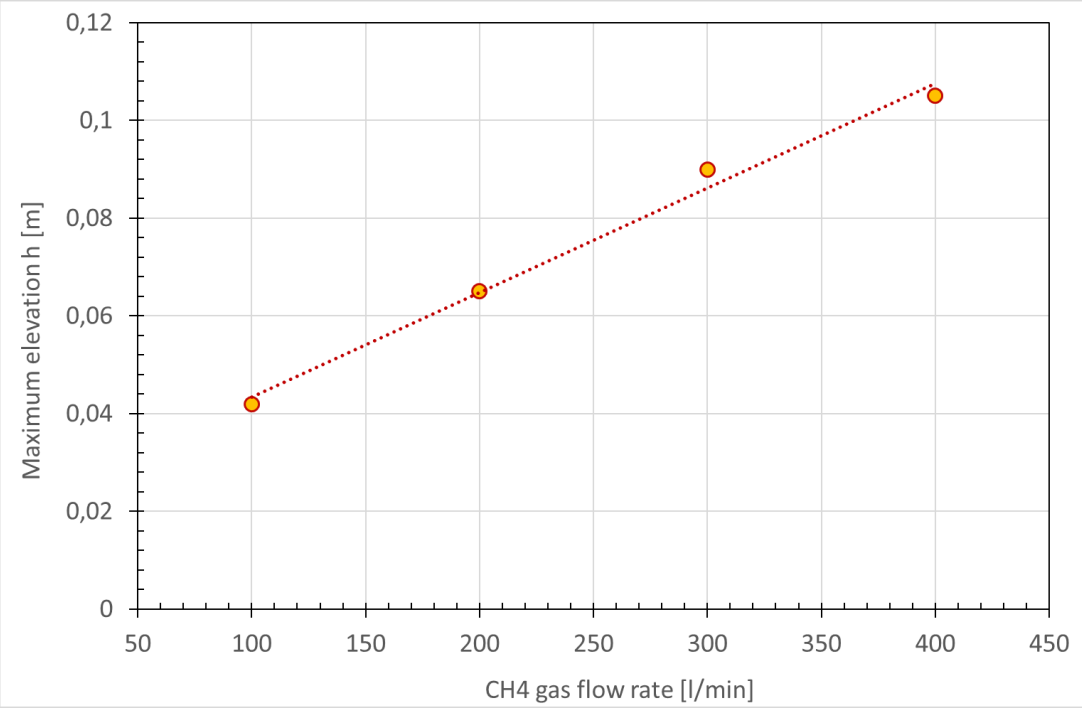

Figure 15: Effect of subsea methane gas flow rate on maximum water surface elevation — experimental results at 2.5 m injection depth

2.2.2.5. Water surface velocity

In the present study, the propagation of water velocity V_{swell} of swell waves generated at the free surface of a seawater pool during the release of methane at four distinct volumetric flow rates Q_v from the bottom of the basin is also examined. The temporal evolution of the free-surface elevation was recorded using a high-resolution Hikvision Mini PTZ dome surveillance camera (Model DS–2DE2A404IW-DE3; $2.8 - 1.2\ mm$ lens). Video sequences were acquired at 25 frames per second with a spatial resolution of 2560×1440 pixels. Each sequence was subsequently segmented into individual frames and digitally processed using MATLAB.

Figure 16 presents the front and lateral views of the experimental apparatus used to release methane gas into a seawater pool; the dome camera was positioned in the upper-right corner of the setup. A fan was installed and operated to direct the methane gas toward the water curtain.

Figure 16: Front view (left image) and lateral side view of the CH_4 gas release experimental setup (right image).

A zoom of the dome camera and the corresponding field of view of the seawater free surface are shown in Figure 17. Upon release at the bottom of the basin, methane rises through the water, forming a bubble plume. On reaching the free surface, the plume interacts with the air–water interface and induces a fountain phenomenon, generating concentric surface waves (swell).

Figure 17: Zoom on the surveillance dome camera (left image) and the observed scene of the seawater free surface variation resulting from the CH_4 gas release at a flow rate Q_v of $100\ l/min$ (right image)

Co-funded by
the European Union

Figure 18 presents a representative temporal sequence of the fountain produced by methane gas release into the seawater pool at a volumetric flow rate of $Q_v = 100\ l/min$, together with the associated swell propagation. As evidenced by the individual frames, the dome camera provides time-resolved imaging of the generated swells. This time-resolved dataset therefore enables the swell propagation velocity along the free surface to be quantified.

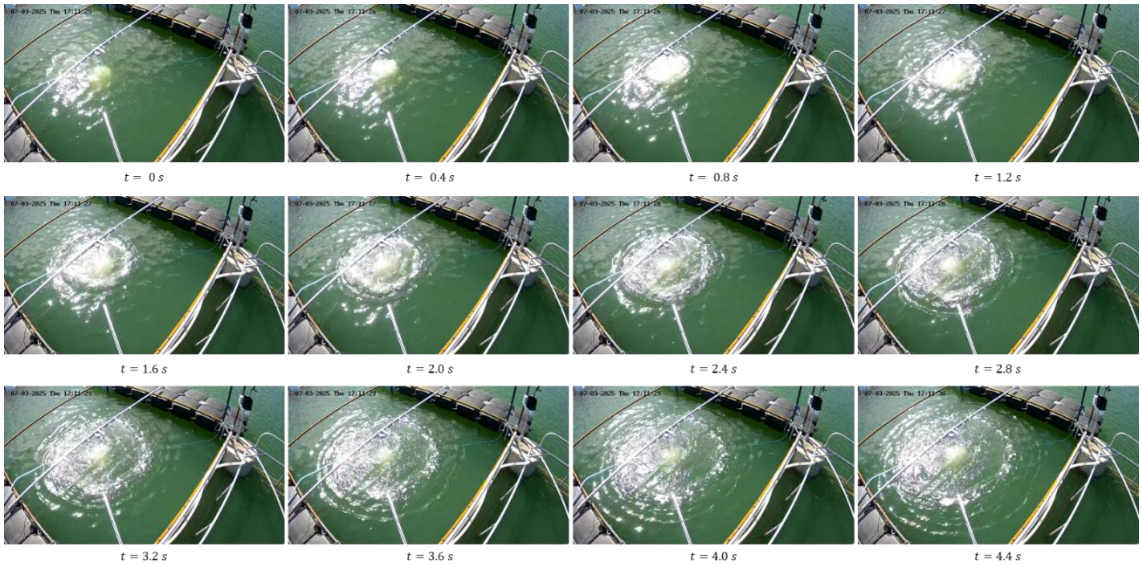

Figure 18: Temporal variation of the seawater free surface resulting from the CH_4 gas release at a flow rate Q_v of $100\ l/min$.

Because regular, nearly circular surface waves are generated on the seawater free surface, selecting an appropriate radial intensity profile — so as to minimize parasitic solar glare in the digital frames — can be used to determine the swell-wave propagation velocity. To this end, two orthogonal axes (Profile 1 and Profile 2 on Figure 19) were defined on the images, and the axis providing the most reliable signal was retained. The two axes, each implemented with a thickness of 10 pixels, are shown in Figure 19a and Figure 19b, respectively. For the image-processing workflow, the RGB frames were first converted to grayscale images, and their intensity levels were adjusted. Then, for each profile, the grayscale intensity was averaged over windows of 10, 20, 30, 40, and 50 pixels in order to obtain the most representative depiction of swell-wave propagation. The resulting grayscale intensity profiles (along both axes), extracted from all frames corresponding to a methane release, were compiled and are reported in Figure 19c and Figure 19d. These space–time representations describe the temporal evolution of the swell wave along the predefined axes, namely Profile 1 and Profile 2. A comparison of the two maps indicates that Figure 19c is affected by a higher noise level than Figure 19d. In Figure 19d, each high-amplitude diagonal ridge (with increasing time)

corresponds to a swell wave propagating along the seawater free surface. The first prominent, rounded trajectory is associated with the initial wave generated by the methane release and is observed in all experiments. Conversely, the lower-amplitude diagonal features with decreasing time are attributed to reflected swell waves originating from the boundaries of the experimental structure.

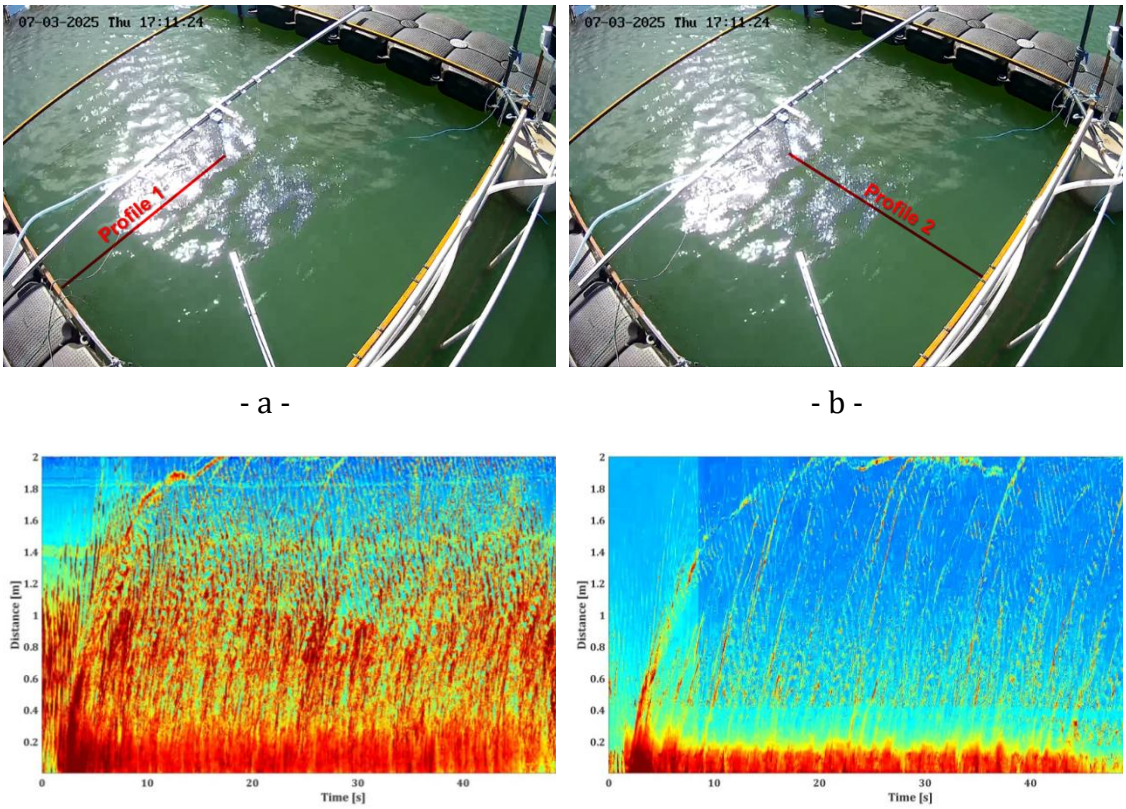

Figure 19: Seawater free surface scene visualized by the dome camera. Images a and b show profiles of interest (Profile 1 and Profile 2) on the scene exploited for investigation of swell velocities. Images c and d show the corresponding time evolution of the grey level profiles (CH_4 gas release flow rate $Q_v = 100\ l/min.$)

For each methane gas release, curves were extracted from the temporal evolution of the swell wave along the predefined axes and were found to be quasi-linear. Consequently, these curves can be accurately approximated by linear regressions, the slope of which corresponds to the mean propagation velocity of the swell V_{swell} along the considered axes.

In the case of a methane release at a flow rate of $100\ l.min^{-1}$, three such curves were extracted, and their corresponding linear regressions are presented in Figure 20. Averaging the resulting velocities yields a representative swell propagation velocity of $V_{swell} = 0.29\ m.s^{-1}$.

The same methodology is applied to the other gas-release flow rates, with the number of velocities included in the averaging process being determined by the quality of the measured temporal evolution of the swell.

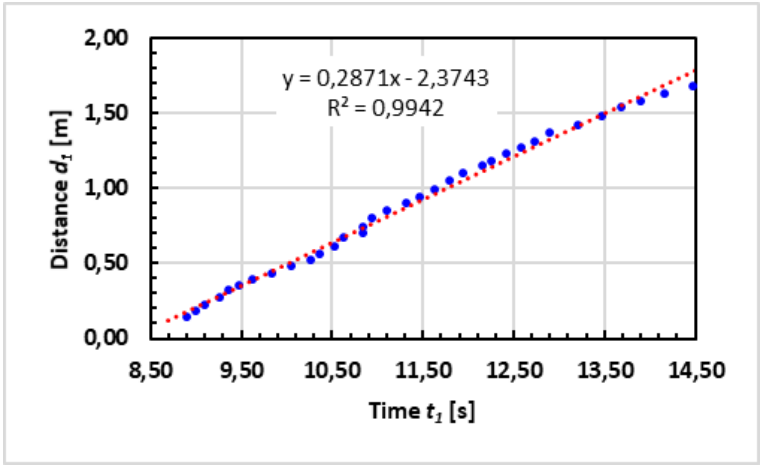

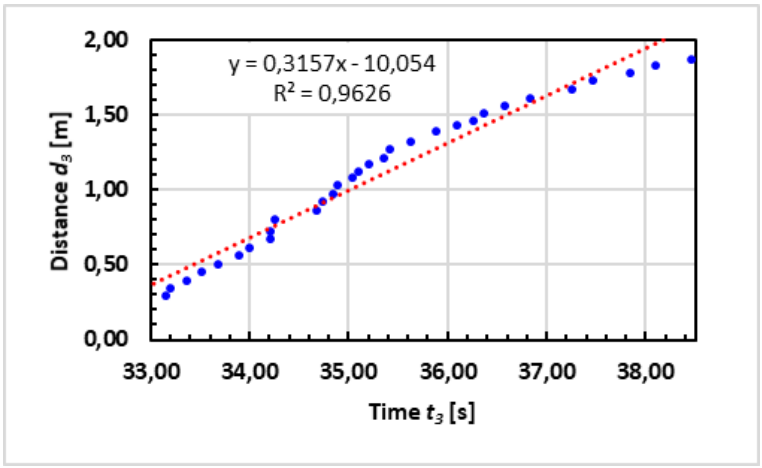

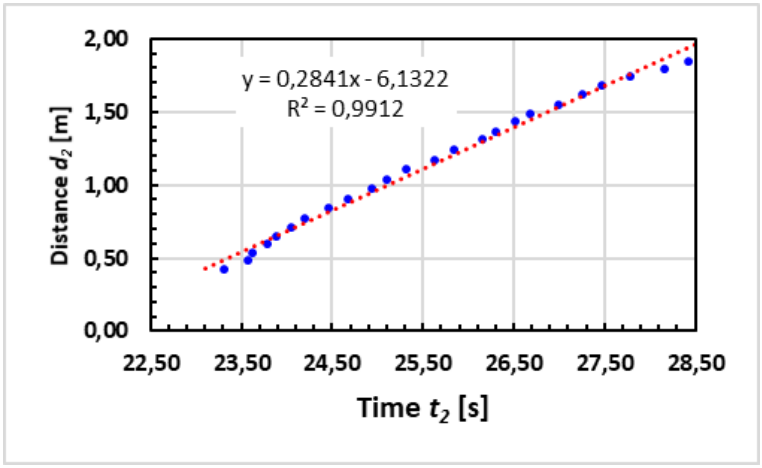

Figure 20: Linear regression of lines extracted from temporal evolution of grey level profiles of the seawater free surface resulting from the CH_4 gas release at a flow rate Q_v of $100\ l/min$.

Co-funded by
the European Union

Two independent series of measurements were conducted for the release of CH_4 gas at four volumetric flow rates: $Q_{v1} = 100\, l.min^{-1}$, $Q_{v2} = 200\, l.min^{-1}$, $Q_{v3} = 300\, l.min^{-1}$ and $Q_{v4} = 400\, l.min^{-1}$. The corresponding time-averaged swell velocities, denoted V_{swell}, are reported in Table 10. The experimental results indicate a systematic increase in the swell velocity V_{swell} with increasing gas flow rate Q_v. The variation of the swell velocity V_{swell} as a function of the gas flow rate Q_v is illustrated in Figure 19. The results reveal a clearly nonlinear dependence of the swell velocity on the gas flow rate. An optimal fit of the experimental data was obtained using a logarithmic relationship, expressed as $V_{swell} = 0.0746 Q_v^{0.29}$, with a regression coefficient of $R^2 = 0.9829$ for Q_v expressed in $l.min^{-1}$ (Figure 21).

	Flow rate Q_v $[m^3.s^{-1}]$	0,0067	0,0050	0,0033	0,0017
	Flow rate Q_v $[l.min^{-1}]$	400	300	200	100
Swell velocities	$V_{swell,1}$	0.40	0.39	0.35	0.29
	$V_{swell,2}$	0.44	0.39	0.37	0.28
	V_{swell}	**0.42**	**0.39**	**0.36**	**0.28**

Table 10: Averaged swell velocities extracted from dome camera frames

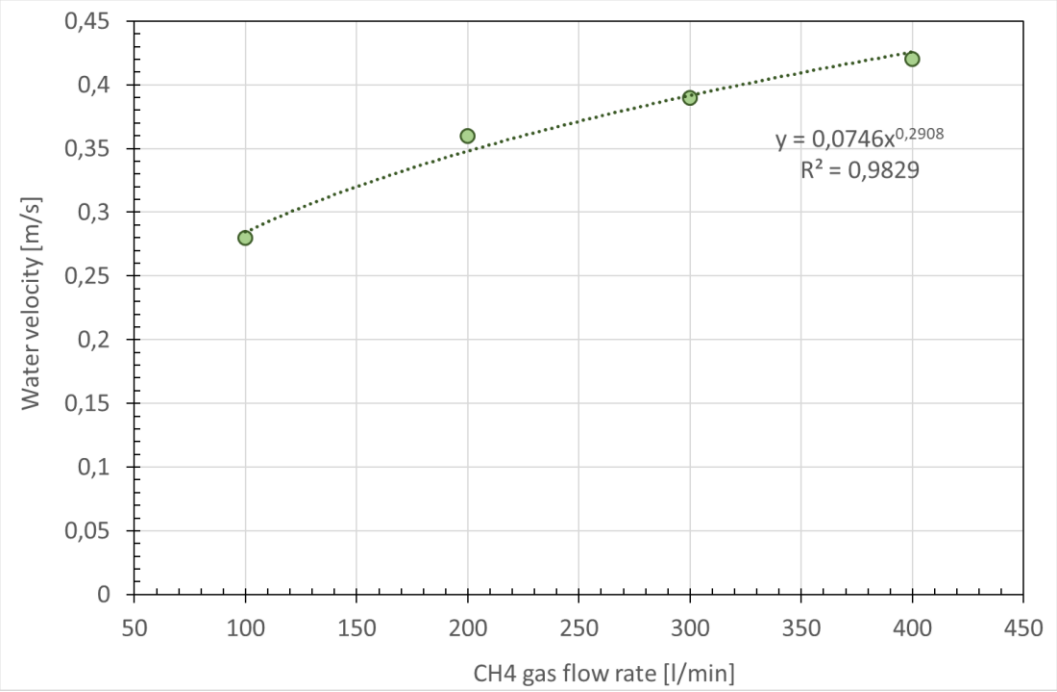

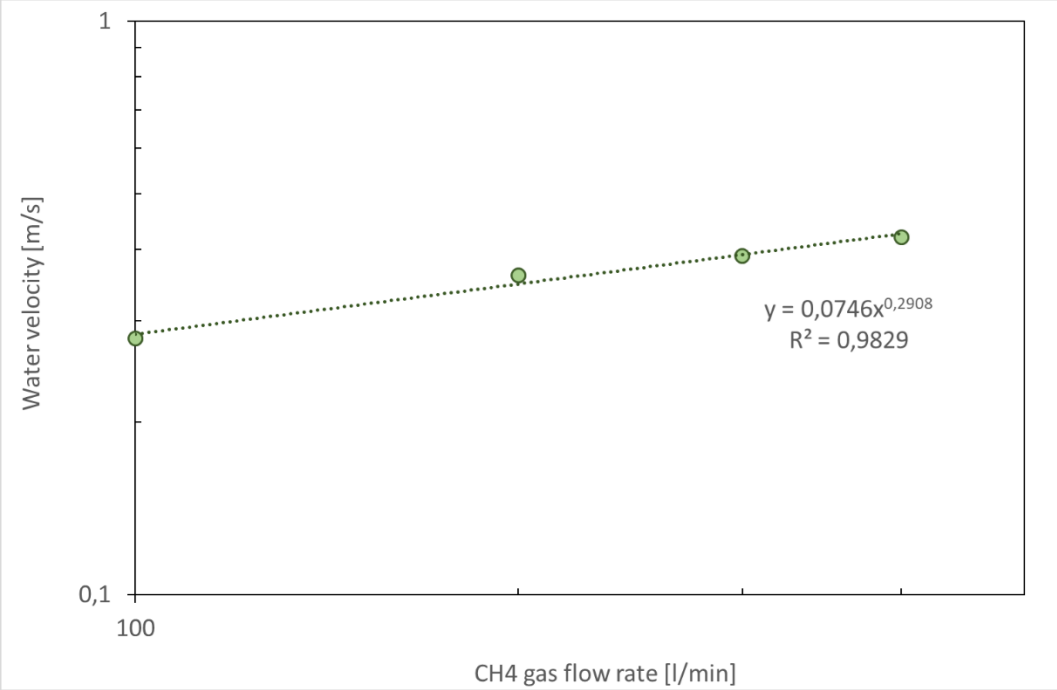

Figure 21: Swell velocity evolution as function of the CH_4 gas release flowrate (in $l.min^{-1}$).

The experimental investigation of methane gas injection in a shallow water basin (2 m depth) reveals a coupled hydrodynamic response governed by buoyancy-driven plume dynamics and strong free-surface constraints. The results highlight a clear distinction between the internal plume behaviour and the surface response.

From a dimensional analysis perspective, the governing parameter of the system is the buoyancy flux:

$$B = g.Q_g \tag{4}$$

where Q_g is the volumetric flow rate and g the gravitational acceleration. In classical turbulent plume theory (Morton–Taylor–Turner framework), the characteristic vertical velocity scale evolves as:

$$U \sim (B.H)^{\frac{1}{3}} \tag{5}$$

which leads to a surface radial velocity scaling:

$$U_r \sim (B.H)^{\frac{1}{3}} \sim Q_g^{\frac{1}{3}} \tag{6}$$

The experimental results are in excellent agreement with this prediction, with a measured exponent close to 0.29. This confirms that the internal flow remains governed by buoyancy-controlled turbulent entrainment. In dimensionless form, the velocity can be expressed as:

$$\frac{U_r}{(g.Q_g)^{\frac{1}{3}}} \approx \text{constant} \tag{7}$$

indicating a robust similarity law consistent with plume theory.

In contrast, the maximum surface elevation η exhibits a much stronger dependence on the gas flow rate, approximately linear ($\eta \sim Q_g$) deviating significantly from the classical scaling:

$$\eta \sim \frac{U^2}{g} \sim Q_g^{\frac{2}{3}} \tag{8}$$

expected for an unconstrained plume impacting a free surface. This discrepancy reveals a transition toward a confinement-controlled regime, in which the surface deformation is not solely governed by the conversion of kinetic energy into potential energy, but by a local accumulation of liquid volume.

This behaviour can be interpreted through a balance between the upward liquid flux induced by the plume and the radial outflow capacity at the surface. The entrained liquid flow rate scales as:

$$Q_{liq} \sim B^{\frac{1}{3}}.H^{\frac{1}{3}} \tag{9}$$

while the radial evacuation scales with *Ur.R*, where *R* is the characteristic plume radius at the surface. In a confined basin, *R* is weakly dependent on Q_g, the limited evacuation capacity leads to a build-up of liquid, yielding:

$$\eta \sim \frac{Q_{liq}}{U_r.R} \sim Q_g \tag{10}$$

This explains the quasi-linear dependence observed experimentally.

A useful dimensionless indicator of this regime shift is the ratio:

$$\frac{U_r^2}{g.\eta} \tag{11}$$

which compares kinetic to potential energy at the surface. In a classical regime, this ratio is of order unity, whereas in the present experiments it decreases with increasing flow rate, indicating that gravitational (potential) energy dominates due to surface accumulation effects.

Overall, the experiments demonstrate that while the subsurface plume dynamics follow classical buoyancy-driven similarity laws, the free-surface response is strongly altered by geometric confinement and finite depth. This leads to a decoupling between velocity and elevation scaling, and highlights the importance of considering system-scale constraints when extrapolating plume behaviour to real configurations such as shallow basins, ports, or offshore releases.

2.2.2.6. Atmospheric gas cloud detection

In addition to the hydrodynamic characterization of the bubble plume, methane dispersion in the gas phase was investigated using a hyperspectral imaging system positioned laterally to the release (Figure 22). This configuration enabled the visualization and quantification of methane concentration fields above the free surface, providing unique insight into the coupling between subsurface plume dynamics and atmospheric dispersion

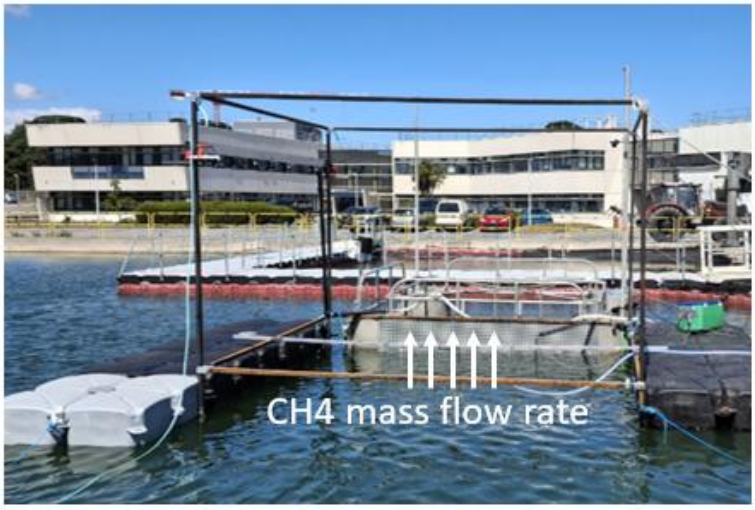

Figure 22: Observation of methane dispersion in the atmosphere. Field of view from Simagaz camera

The hyperspectral measurements reveal that methane does not disperse as a steady, homogeneous plume, but rather as highly intermittent and structured turbulent puffs (Figure 23a). These structures originate directly from the unsteady release of gas at the free surface, which is itself controlled by the dynamics of the bubble plume and the associated surface deformation. In particular, the strong agitation and localized upwelling observed at the surface generate episodic gas releases, leading to coherent methane clouds that are then advected and diluted by the ambient airflow.

A key feature observed in the experiments is the dominant influence of the ambient wind, blowing from the left-hand side of the (Figure 23b). This crossflow strongly affects the near-field dispersion by advecting the methane puffs horizontally while simultaneously pressing them toward the water surface. As a result, the structures remain confined close to the interface over a certain distance, forming a shallow, elongated cloud before progressively lifting and diluting into the atmosphere. This near-surface confinement enhances local concentration levels and prolongs the residence time of methane in the vicinity of the source, compared to what would be expected under quiescent conditions.

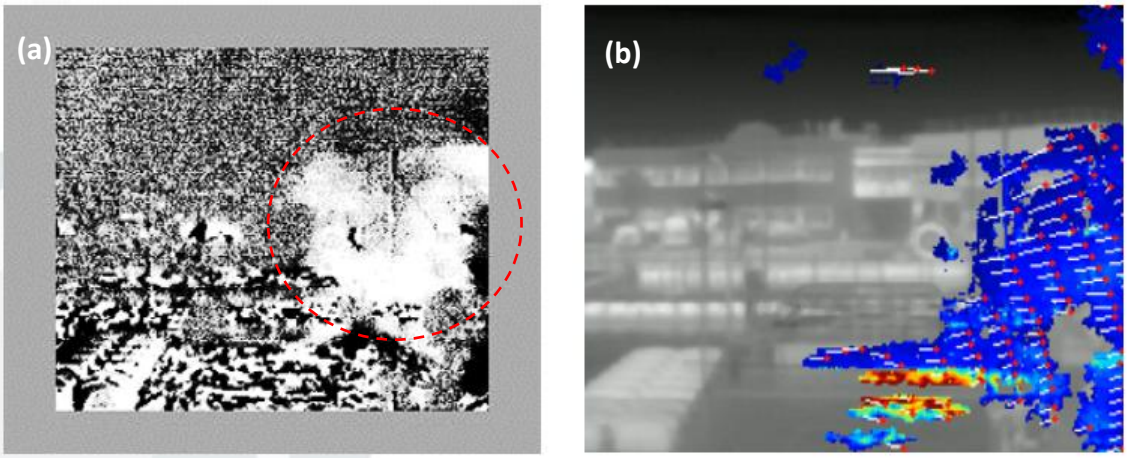

Figure 23: Observation of methane cloud with hyperspectral Simagaz camera (red dot circle on picture (a)). Observation of the methane cloud dispersion (b)

The spatial and temporal characteristics of these gas structures are therefore governed by a coupled interaction between:

- the unsteady release dynamics at the free surface,
- the buoyancy and initial momentum of the gas phase
- the shear and advection induced by the ambient wind field.

From a scaling perspective, while the total methane emission rate is directly linked to the injected gas flow rate, the effective dispersion is controlled by this competition between buoyancy (tending to lift the gas) and wind-induced shear (tending to advect and confine it near the surface). This highlights that near-field dispersion cannot be described using steady-state Gaussian assumptions, but instead requires a transient and shear-influenced framework, particularly in the presence of even moderate crossflow.

Overall, the combined analysis demonstrates a strong coupling between subsurface gas injection, free-surface hydrodynamics, and atmospheric dispersion. While the plume dynamics follow classical buoyancy scaling, the surface processes control the temporal structure of gas release, and the ambient wind governs the subsequent transport and near-surface confinement of methane, ultimately shaping the dispersion patterns observed above the water.

The temporal evolution of the methane mass flow rate, measured using the Simagaz hyperspectral camera, shows significant unsteady behaviour in the gas emission at the free surface (Figure 24). The data show pronounced fluctuations over time, with instantaneous mass flow rates ranging from approximately 0.5 to 6.5 g/s, and an average value around 2.5–3 g/s. These variations highlight the highly intermittent nature of the gas release process, which is consistent with the previously observed turbulent plume dynamics and surface agitation. The fluctuations in mass flow rate can be attributed to a combination of mechanisms, including the intrinsic unsteadiness of the bubble plume, the episodic bursting of gas at the surface, and the influence of wind-induced shear. In

particular, the crossflow wind contributes to modulating the apparent emission by intermittently dispersing and redistributing methane near the surface, leading to temporal variability in the detected signal. This suggests a strong coupling between underwater hydrodynamics, surface processes, and atmospheric transport, where the effective gas release is not steady but governed by transient interactions across the air–water interface. Such behaviour reinforces the need to consider time-resolved emission rates rather than steady averages when assessing gas dispersion and associated risks.

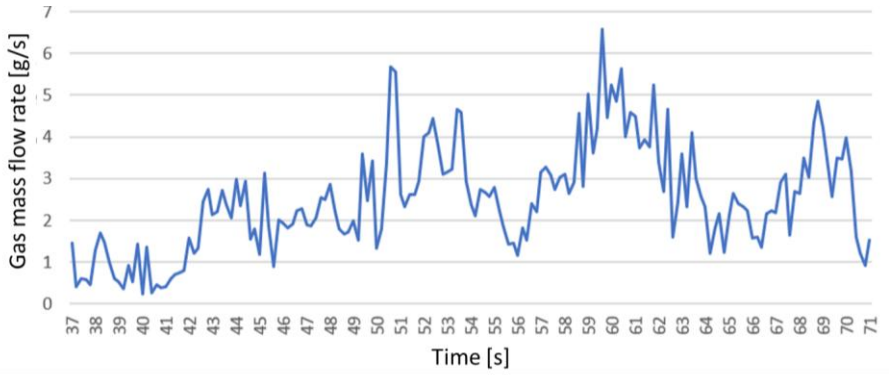

Figure 24: Illustration of the temporal variation of atmospheric methane gas mass flow rate measured with hyperspectral Simagaz camera

A comparison between the mean gas injection flow rates at the underwater nozzle and the mean methane mass flow rates measured by the hyperspectral camera shows a generally good agreement across most operating conditions (Table 5). This indicates that, despite the complex multiphase processes involved (bubble rise, surface release, and atmospheric dispersion), the hyperspectral measurements provide a reliable estimate of the effective gas emission to the atmosphere. However, a notable discrepancy is observed for the 300 L/min case (corresponding to an expected mass flow rate of approximately 3.33 g/s), for which the hyperspectral system records a significantly lower value (around 1.48 g/s). This deviation is most likely attributable to stronger wind effects during this specific test, which enhanced the lateral dispersion of the methane cloud and reduced the fraction of gas captured within the camera's field of view. In this configuration, the crossflow not only advects the gas plume away from the measurement region but also increases dilution and intermittency, leading to an underestimation of the actual emission rate. In addition, it is important to emphasize that the accuracy of hyperspectral measurements strongly depends on the viewing geometry: the camera optical axis should be as perpendicular as possible to the plane of the gas cloud in order to maximize the detected signal and minimize geometric distortions. Any misalignment can lead to partial sampling of the plume and thus to further underestimation of the mass flow rate. This result highlights the sensitivity of optical measurement techniques to both environmental conditions and measurement configuration, and underscores the importance of carefully controlling wind effects and sensor positioning when interpreting remote sensing data of gas release

Mean injection flow rate [L/min]	Mean injection flow rate [g/s]	Mean flow rate measured by camera [g/s]
100	1,11	0,94
200	2,22	2,53
300	3,33	1,48
400	4,60	4,73

Table 11: List of experimental devices and sensors used for ammonia tests performed in July 2025 (basin trial)

This chapter presented an experimental investigation of underwater gas release dynamics and the associated hydrodynamic and atmospheric dispersion phenomena, conducted at the CEDRE basin facility. Two gases were studied — methane and ammonia — at various volumetric flow rates, using a comprehensive instrumentation system including thermocouples, pressure sensors, flow controllers, acoustic velocimeters, visible and hyperspectral cameras, and explosimeters.

For methane releases, the experimental results demonstrated a clear and monotonic increase in free-surface elevation with increasing gas flow rate, well described by a Gaussian model. The maximum surface elevation followed a quasi-linear relationship with flow rate, ranging from approximately 4.2 cm at 100 L/min to 10.5 cm at 400 L/min, with an excellent coefficient of determination ($R^2 = 0.9996$). Two Gaussian formulations were evaluated: a zero-baseline model (Gaussian A) and a variable-baseline model (Gaussian B), the latter providing improved agreement with the experimental median profiles, particularly at higher flow rates where the zero-baseline model showed increasing divergence at the profile tails.

The analysis of swell wave propagation at the free surface revealed a nonlinear dependence of the swell velocity on the gas flow rate, best described by a power-law relationship ($V_{swell} = 0.0746\ Q_v^{0.29}$, $R^2 = 0.9829$). This measured exponent of approximately 0.29 is in excellent agreement with classical buoyancy-driven turbulent plume theory, which predicts a surface radial velocity scaling as $Q_v^{1/3}$. In contrast, the maximum surface elevation exhibited a quasi-linear dependence on flow rate, deviating significantly from the classical $Q_v^{2/3}$ scaling expected for an unconstrained plume. This discrepancy was interpreted as a transition toward a confinement-controlled regime, in which the limited radial evacuation capacity of the confined basin leads to a local accumulation of liquid at the surface, decoupling the velocity and elevation scaling laws.

Atmospheric methane dispersion above the free surface was characterized using a hyperspectral Simagaz camera. The measurements revealed a highly intermittent and structured gas emission, driven by the unsteady dynamics of the bubble plume and the episodic bursting of gas at the air-water interface. Ambient wind was identified as a

dominant factor controlling near-field dispersion, advecting the methane puffs horizontally while confining them close to the water surface, thereby enhancing local concentration levels and prolonging residence times near the source. The temporal evolution of the methane mass flow rate showed pronounced fluctuations, with instantaneous values ranging from approximately 0.5 to 6.5 g/s around a mean of 2.5–3 g/s, confirming the strongly transient nature of the emission process. A generally good agreement was found between the injected flow rates and the hyperspectral measurements, with the exception of the 300 L/min test, where stronger wind conditions led to underestimation of the detected mass flow rate due to lateral dispersion beyond the camera's field of view.

Overall, the experiments demonstrated a strong coupling between subsurface gas injection dynamics, free-surface hydrodynamics, and atmospheric dispersion. While the subsurface plume behaviour follows classical buoyancy-driven similarity laws, the free-surface response is strongly influenced by geometric confinement, and the subsequent atmospheric transport is governed by the interplay between gas buoyancy and ambient wind shear.

2.2.3. Ammonia experiments

2.2.3.1. Experimental setup

The ammonia test campaign was conducted at the CEDRE basin facility (Figure 2). Based on the results obtained in November 2024, the injection nozzle diameter was increased from 10 mm to 20 mm internal diameter in order to achieve higher gas flow rates. The nozzle was positioned at the center of the basin, 10 cm below the water surface. Three flow rates were investigated (100, 200 and 260 L/min), each sustained for approximately one to two minutes. Concentration measurements were performed using two explosimeters, one placed vertically above the release point and the other located 3 m away (Figure 3). A full list of the instrumentation used is provided in *Table 5*.

For all three flow rates, the ammonia release produced no observable impact at the water surface — neither a fountain effect nor any significant variation in the measured water current was detected. However, a white precipitate formed in the water column, consistent with observations from previous experiments. This precipitate had been difficult to identify during previous test campaign (November 2024).

Figure 25 presents the pressure and temperature measurements recorded along the release line during the three successive flow rate conditions. The pressure at the cylinder outlet (solid blue curve) shows a sharp increase at the onset of each release, reflecting the initial pressurization of ammonia at approximately 8 bar within the cylinder, followed by a stabilization during sustained injection. The gas temperature at the cylinder outlet (dashed orange curve) exhibits a progressive decrease with increasing flow rate, consistent with adiabatic expansion of the gas through the piping system (Joule-Thomson effect). In contrast, the temperature measured at the nozzle exit (solid

orange curve) shows a systematic increase with flow rate, indicative of the exothermic dissolution of ammonia in seawater occurring at the injection point.

The contrasting thermal behaviours observed at the two measurement locations — cooling at the cylinder outlet and heating at the nozzle exit — confirm that the dominant thermodynamic process at the air-water interface is the exothermic dissolution of ammonia in seawater, which more than compensates for the upstream cooling induced by gas expansion (Figure 26). Furthermore, temperature fluctuations at the nozzle exit were observed to intensify with increasing flow rate, particularly at 260 L/min, suggesting the onset of a turbulent or slug flow regime within the injection pipe at higher flow conditions. The average, minimum and maximum temperatures recorded at each flow rate are summarized in Table 12.

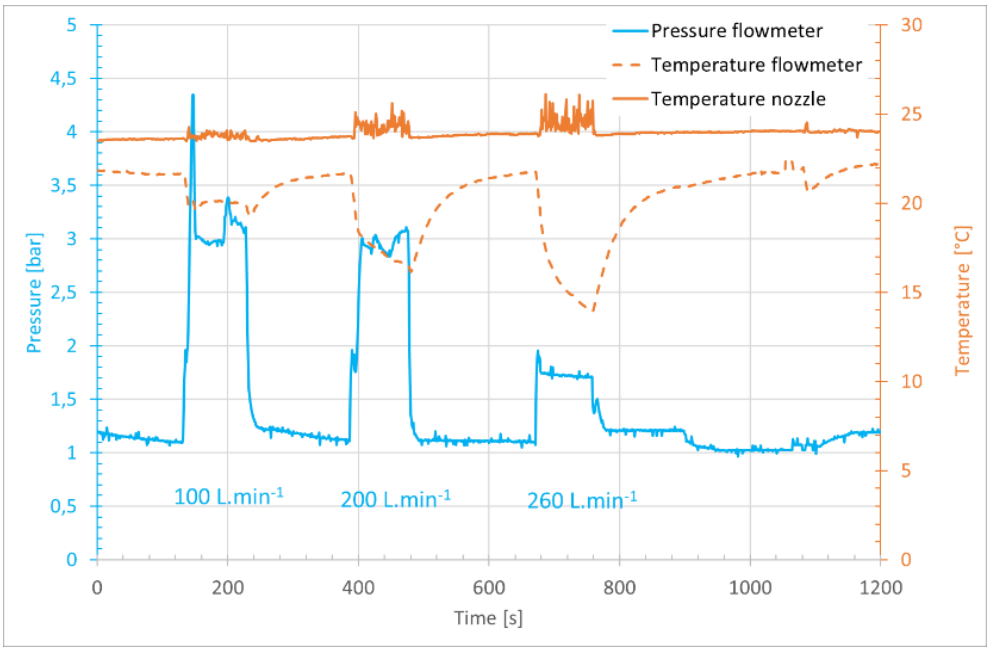

Figure 25: Temporal pressure and temperature histories recorded along the ammonia release line during the three successive injection tests (100, 200 and 260 L/min). Solid blue curve represents the pressure at the cylinder outlet and dashed orange curve represents the gas temperature at the cylinder outlet.

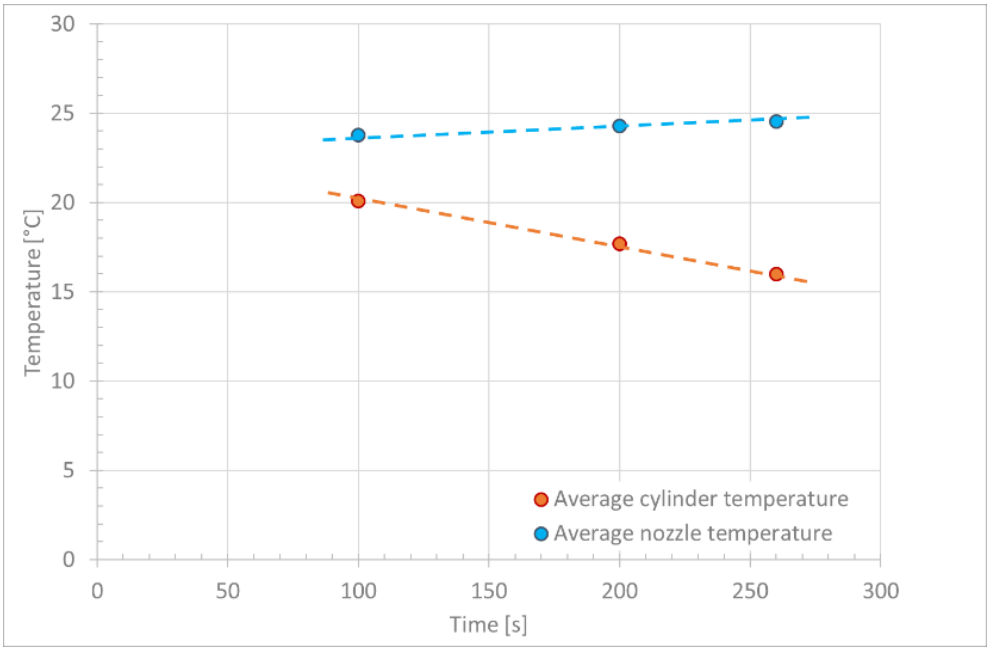

Figure 26: Variation of average temperatures at the bottle outlet and injection nozzle for ammonia emissions at different flow rates

Table 12: Variation of average, minimum and maximum temperature at cylinder exit and nozzle exit for three different flow rates

Value	Temperature [°C]	Flow rate [L.min^{-1}]		
		100	200	300
Average	at cylinder exit	20.07	17.67	16.0
	at nozzle exit	23.78	24.28	24.52
Min	at cylinder exit	19.56	16.53	13.98
	at nozzle exit	23.47	23.60	23.78
Max	at cylinder exit	21.68	21.7	21.75
	at nozzle exit	24.28	25.62	26.12

The Figure 27 presents the ammonia injection pressure (blue curve) alongside the atmospheric ammonia concentration measured 30 cm above the water surface, directly above the release point, by the Dräger explosimeter (red curve). Despite the high solubility of ammonia in seawater, the sensor recorded significant atmospheric

concentrations, with a peak value of approximately 295 ppm. It should be noted that this value corresponds to the upper measurement limit of the Dräger explosimeter, meaning that the actual atmospheric concentration may have been equal to or greater than this value during the peak events. A striking feature of these measurements is that the concentration peaks occurred well after the injection phases had concluded, as evidenced by the pressure returning to its baseline value prior to any detectable atmospheric release. This temporal decoupling between the injection and the atmospheric detection confirms that the measured gas does not originate directly from the injection flow, but rather from a secondary release from the water body itself.

Two hypotheses are proposed to explain this delayed atmospheric release. The first hypothesis involves volatilization of dissolved ammonia from the upper layers of the water column, either through progressive outgassing as the dissolved ammonia equilibrates with the atmosphere, or through the delayed arrival of a saturated water plume at the surface. The second hypothesis relates to instrumental factors, including a possible synchronization offset between data loggers or a slow sensor recovery time following exposure to high humidity or elevated concentration levels. However, the clear correlation between the pressure baseline and the concentration peaks strongly supports the first hypothesis, suggesting that volatilization is the dominant mechanism.

From a safety perspective, the peak atmospheric concentration of approximately 295 ppm is particularly significant. This threshold of 295 ppm approaches the Immediately Dangerous to Life or Health (IDLH) level of 300 ppm defined by NIOSH for ammonia, at which 30 minutes of exposure may cause irreversible health effects or prevent self-evacuation. The fact that such concentrations — potentially underestimated due to sensor saturation — were detected 30 cm above the water surface after the active injection had ceased highlights a critical and often overlooked hazard: the delayed volatilization of dissolved ammonia can generate a toxic atmosphere in the immediate vicinity of the water surface even in the absence of any ongoing gaseous release, with significant implications for operational safety in confined or semi-confined environments.

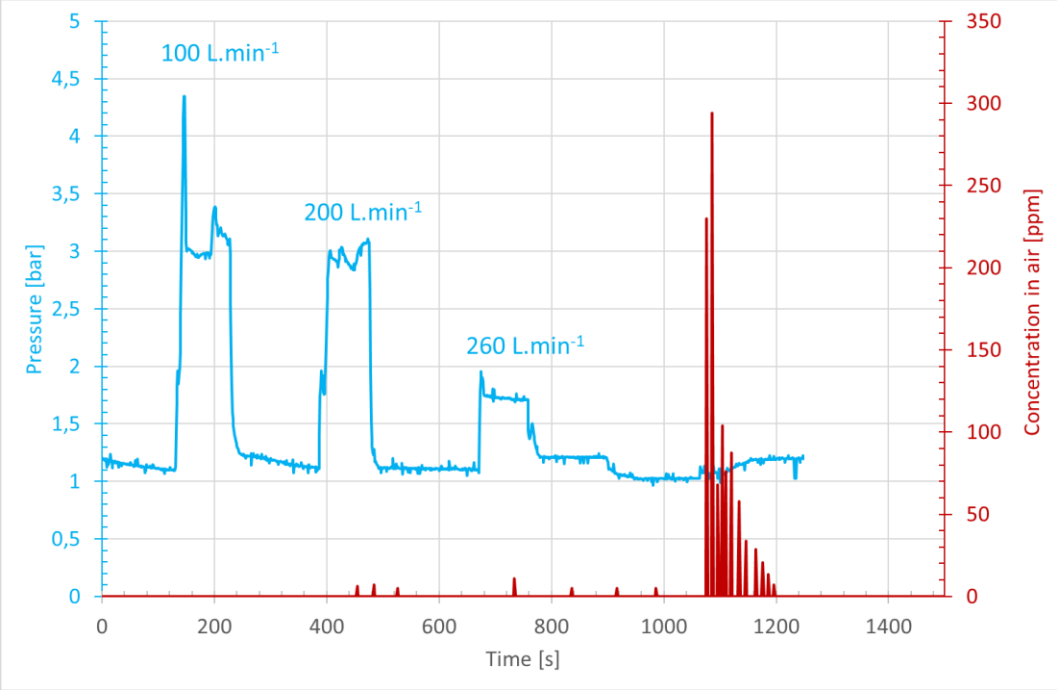

Figure 27: Temporal histories of ammonia injection pressure (blue curve) and atmospheric ammonia concentration measured 30 cm above the water surface directly above the release point (red curve) during the three successive injection tests (100, 200 and 260 L/min).

The Figure 28 illustrates the evolution of seawater pH in response to subsea ammonia injection. Prior to the releases, the seawater pH remained stable at a baseline value of approximately 8.6. No significant variation was observed during the 100 and 200 L/min injection phases. However, following the 260 L/min release, a sharp and sustained increase in pH was recorded, reaching a peak value of approximately 9.3. This alkalinisation is a direct consequence of the dissolution of ammonia in seawater, which produces hydroxide ions (OH^-) through the following equilibrium reaction:

$$NH_3 + H_2O \rightleftharpoons NH_4^+ + OH^- \quad (12)$$

thereby increasing the pH of the surrounding water.

Consistent with the atmospheric concentration measurements, a significant time lag was observed between the end of the injection and the onset of the pH rise, with the pH remaining elevated for several hundred seconds after the gas flow had ceased. This delayed response suggests that the pH sensor captured the arrival of a concentrated dissolved ammonia plume that persisted in the measurement area due to slow ambient currents or localized saturation of the water column, further confirming that ammonia remains chemically active in the aqueous phase well after the physical injection has ended.

From an environmental and safety perspective, the recorded pH increases to 9.3 is of concern. At this level, seawater alkalinity can damage the protective mucus layers of fish and adversely affect the eggs and larvae of crustaceans, posing a significant risk to

marine organisms in the vicinity of the release. For human exposure, while a pH of 9.3 is considerably less corrosive than strong alkaline substances, it remains irritating to skin and potentially harmful to eyes upon direct contact, highlighting the importance of appropriate protective measures during ammonia release operations.

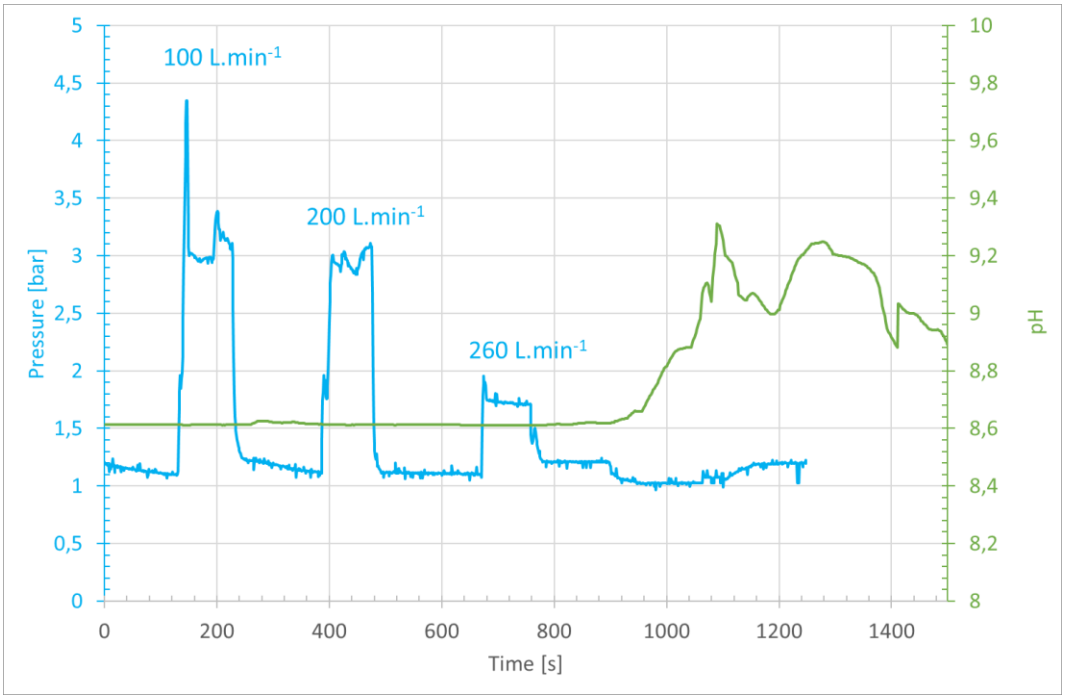

Figure 28: Temporal histories of ammonia injection pressure (blue curve) and seawater pH (green curve) measured in the basin during the three successive injection tests (100, 200 and 260 L/min)..

Figure 29 presents a direct comparison between the seawater pH and the atmospheric ammonia concentration measured above the water surface throughout the entire test campaign. The combined visualization of these two quantities provides compelling evidence of a causal relationship between aqueous ammonia saturation and atmospheric re-volatilization. During the initial injection phases, while the seawater pH remained at its baseline value of approximately 8.6, no significant atmospheric ammonia concentration was detected. However, once the pH exceeded approximately 8.8, a pronounced off-gassing event was observed, with atmospheric concentrations peaking at approximately 295 ppm — the upper measurement limit of the Dräger explosimeter. This behaviour suggests the existence of a critical pH threshold beyond which the buffering capacity of seawater is overcome, shifting the dissolution-volatilization chemical equilibrium toward the gas phase and triggering significant ammonia release at the air-water interface.

The temporal synchronization between the pH surge and the atmospheric concentration peaks further supports this interpretation, indicating that the high alkalinity of the

dissolved ammonia plume is the primary driver of volatilization at the surface. These findings have direct implications for safety protocols in environments where subsea ammonia releases may occur: continuous monitoring of seawater pH could serve as an early warning indicator of imminent toxic gas release at the surface, potentially providing critical reaction time before atmospheric concentrations reach hazardous levels.

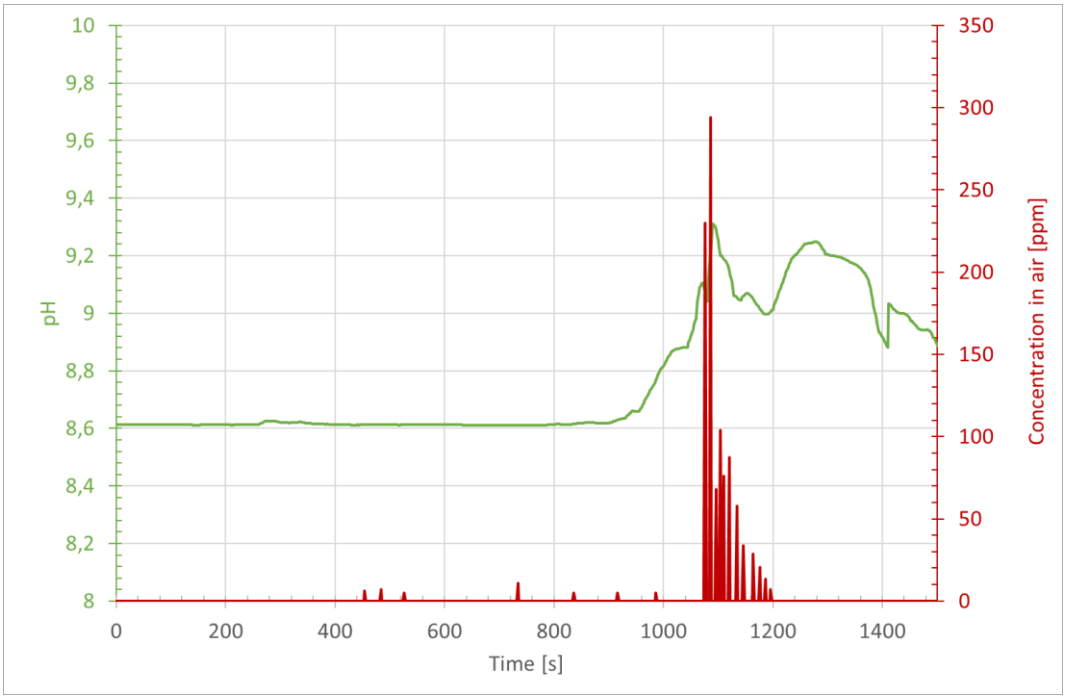

Figure 29: Simultaneous time histories of seawater pH (green curve) and atmospheric ammonia concentration measured 30 cm above the water surface (red curve) for the test campaign.

Experimental campaigns conducted in July 2025 in CEDRE's outdoor basin investigated the physical and chemical behaviour of underwater ammonia releases at a depth of 10 cm below the water surface. The results revealed that the dissolution of ammonia in seawater is governed by an exothermic process, with temperatures at the nozzle exit reaching up to 26.12°C, effectively overriding the upstream cooling induced by adiabatic gas expansion. Despite the absence of any visible surface disturbance — no fountain effect or measurable water current variation was observed at any of the tested flow rates — the chemical impact on the water body was significant. The seawater pH increased from a baseline of 8.6 to a peak value of 9.3, reflecting the progressive saturation of the water column with dissolved ammonia and the associated production of hydroxide ions, which substantially increases the fraction of toxic un-ionized ammonia in solution.

Atmospheric monitoring above the water surface revealed an important safety subject, with ammonia concentrations reaching the upper measurement limit of the Dräger explosimeter (~295 ppm), approaching the IDLH threshold of 300 ppm defined by

NIOSH, at a height of only 30 cm above the surface. It is important to noted taht these peak concentrations were recorded with a significant time delay relative to the end of the injection phases, confirming that the dominant source of atmospheric ammonia was not direct release during injection but rather secondary volatilization from the dissolved ammonia plume persisting in the water column. The synchronization between the pH surge above 8.8 and the onset of atmospheric concentration peaks suggests that this pH value constitutes a critical threshold beyond which the buffering capacity of seawater is overcome and volatilization becomes significant. This finding establishes seawater pH monitoring as a potentially valuable predictive indicator for imminent toxic gas release at the surface, with important implications for operational safety in marine environments where subsea ammonia discharges may occur.

2.3. Medium scale experiments of liquid ammonia release above water surface

2.3.1. Ammonia release

2.3.1.1. Experimental setup

This experimental phase was conducted at the SDIS 29 training site and aimed to characterize the thermal and chemical dynamics of a pressurized liquid ammonia release onto a water surface. The experimental configuration was closely analogous to that used for the cryogenic nitrogen release campaign, with liquid ammonia discharged from a pressurized cylinder onto the water surface of the same 3 m × 3 m portable pool (Justrite Rigid-Lock QuickBerm®), filled to a depth of 19 cm. The ammonia release nozzle was positioned 10 cm above the water surface, at one end of the pool. Given the acute toxicity of ammonia, the entire trial was conducted under remote control to ensure personnel safety.

Temperature measurements were performed using a network of 12 Type-T thermocouples deployed along the central axis of the pool, aligned with the release axis, as illustrated in Figure 30 and Figure 32. At each measurement position, two sensors were deployed simultaneously: one in air, placed 15 cm above the water surface, and one in water, placed 5 cm below the water surface. The spatial configuration included a reference sensor (T_0) positioned 25 cm upstream of the release point and a near-field sensor (T_1) located 5 cm downstream of the nozzle, followed by sensors spaced at regular 40 cm intervals along the release axis (Figure 31).

In addition to the thermocouple network, the chemical impact of the ammonia release on the water body was monitored using a WiMo probe for continuous pH and temperature measurements, complemented by an NH_4^+ ion-selective probe to quantify the concentration of dissolved ammonium ions in the water column. The experiment was further instrumented with a comprehensive imaging suite comprising visible light

surveillance cameras, a FLIR infrared camera coupled with an ONERA ammonia-specific detector, and a SDIS 29 drone equipped with thermal imaging, providing multi-scale visualization of both the vapor cloud dispersion and the thermal footprint of the liquid ammonia evaporation at the water surface.

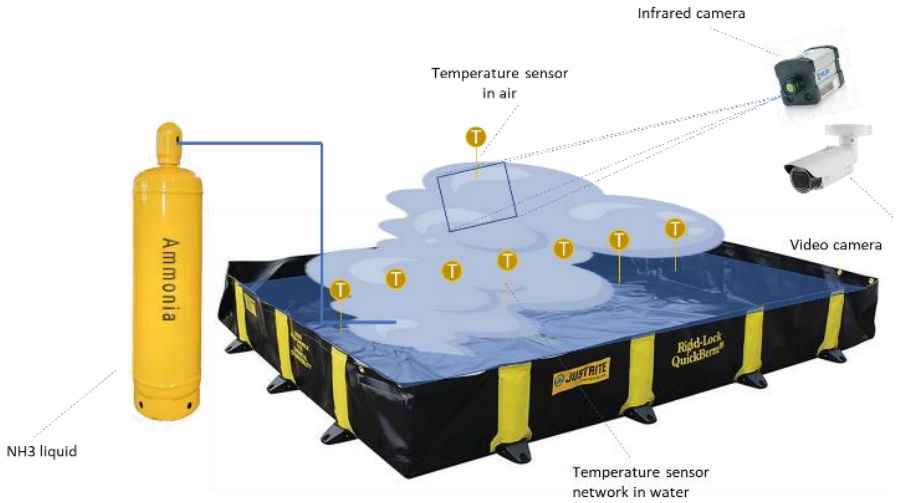

Figure 30: Schematic overview of the experimental setup for the pressurized liquid ammonia release campaign. Liquid ammonia is discharged from a pressurized cylinder onto the water surface of a 3 m × 3 m portable pool. Temperature measurements are performed by a network of Type-T thermocouples deployed along the release axis, with sensors positioned 15 cm above the water surface (T_air) and 5 cm below the water surface (T_water). The experiment is monitored by a visible light camera, a FLIR infrared camera with an ONERA ammonia-specific detector, and a SDIS 29 drone equipped with thermal imaging.

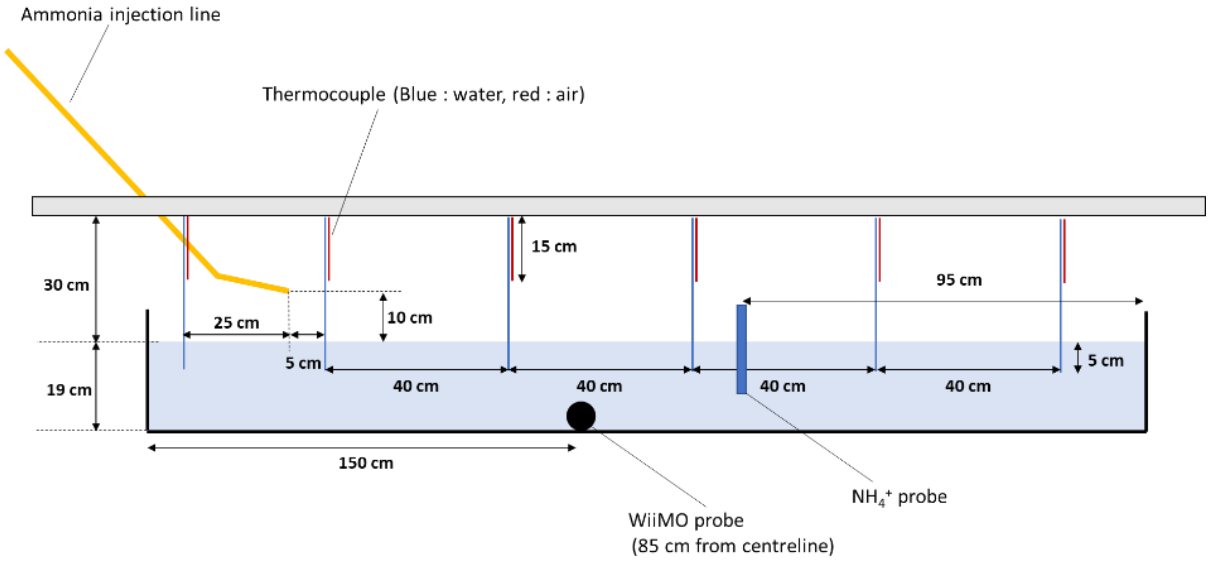

Figure 31: Schematic side view of the thermocouple array and chemical probe deployment along the central axis of the pool. Air temperature sensors (red) are positioned 15 cm above the water surface and water temperature sensors (blue) are placed 5 cm below the water surface. A WiMo pH and temperature probe and an NH_4^+ ion-selective probe are additionally deployed in the water column

Co-funded by
the European Union

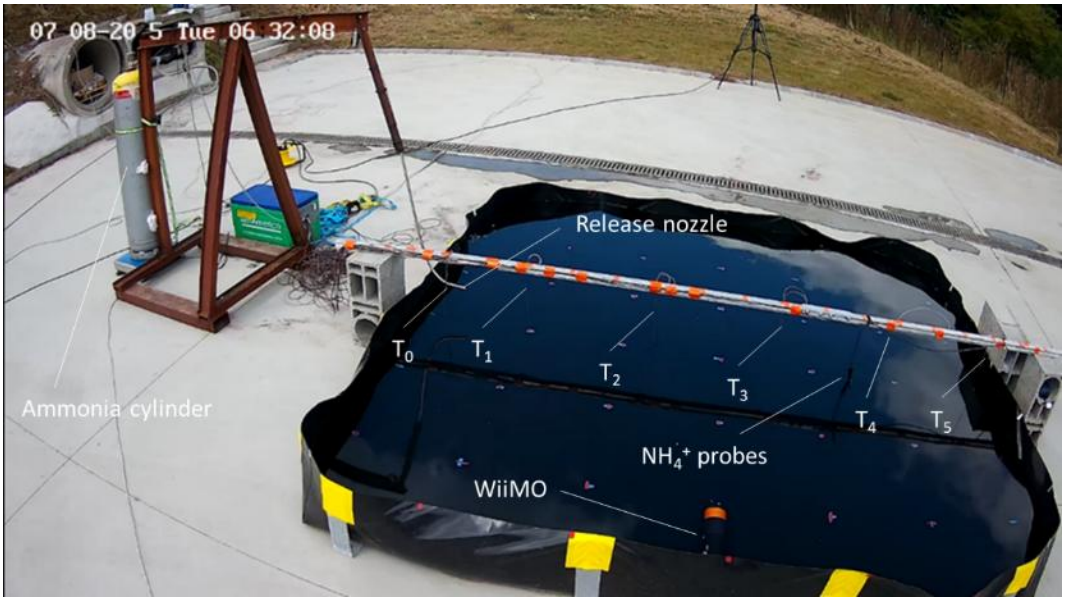

Figure 32: Photograph of the experimental setup at the SDIS 29 training site prior to the pressurized liquid ammonia release. The pressurized ammonia cylinder and the remote-controlled release mechanism are visible on the left. The thermocouple support rail is mounted along the central axis of the pool, with sensor positions T_0 to T_5 indicated. The WiMo probe and NH_4^+ probes are visible within the pool

2.3.1.2. Analysis of experimental results

Figure 33 illustrates the pressurized liquid ammonia discharge at the water surface as recorded by the surveillance camera during the test. The image clearly shows that ammonia exits the nozzle as a dense white plume, characteristic of a two-phase liquid-gas mixture resulting from the rapid adiabatic expansion of the pressurized fluid at the discharge valve and within the supply line. This expansion induces significant cooling of the gas phase through the Joule-Thomson effect, suggesting that the thermocouples located immediately downstream of the nozzle are likely to record very low, potentially sub-zero temperatures during the initial phase of the release, before the exothermic dissolution reaction begins to contribute heat.

The white appearance of the plume is attributed to the instantaneous condensation of atmospheric water vapor in the vicinity of the nozzle. As liquid ammonia expands from the pressurized cylinder to atmospheric pressure, the resulting flash-cooling drops the local gas temperature well below the dew point of the surrounding air, causing water vapor to condense into fine liquid droplets and forming a visible fog. Due to the extreme hygroscopicity of ammonia, the gas dissolves rapidly into these droplets, forming an ammonium hydroxide aerosol. This dissolution process is exothermic and partially offsets the initial cooling induced by gas expansion before the plume reaches the water surface. It is therefore important to note that the air temperature sensors are not measuring dry ambient air but are instead immersed in this two-phase aerosol mixture,

capturing the complex thermal balance between expansion cooling and dissolution heating.

Although pure ammonia gas is lighter than air under ambient conditions, the cold and moisture-laden aerosol formed at the nozzle exit is denser than the surrounding atmosphere, explaining the ground-hugging behaviour of the plume visible in the image. This density-driven behaviour promotes prolonged contact between the ammonia cloud and the water surface, maximizing the air-water interaction and facilitating ammonia dissolution into the pool. The alignment of the plume with the thermocouple array axis is also clearly visible, confirming that both the air and water sensors are directly exposed to the ammonia cloud, which is an essential condition for the interpretation of the thermal and chemical measurements recorded during the experiment.

Figure 33: Aerial view of the pressurized liquid ammonia release onto the water surface, recorded by the surveillance camera during the test. A dense white plume, characteristic of a two-phase mixture generated by the adiabatic expansion of liquid ammonia at the nozzle exit, propagates along the thermocouple array axis, ensuring direct exposure of both air and water sensors to the ammonia cloud.

A close-up observation of the injection nozzle during the release reveals significant frost accumulation on the outer surface of the supply pipe, as illustrated in Figure 34. This icing is direct evidence that pipe wall temperatures dropped well below 0°C, driven by the adiabatic expansion of the pressurized ammonia upstream of the nozzle exit. Under these conditions, partial re-liquefaction of ammonia within the piping system is thermodynamically plausible, and the presence of a distinct circular impact zone on the water surface confirms that ammonia enters the pool at least partially in liquid form rather than exclusively as a gas or aerosol.

This transition from a two-phase plume to localized liquid droplets impacting the water surface has important implications for the local energy balance at the point of impact. The direct contact of liquid ammonia — at its boiling point of approximately −33°C — with the warmer seawater concentrates the exothermic dissolution reaction at a well-defined location, potentially generating a sharp thermal contrast between the intense

local cooling induced by liquid ammonia evaporation and the subsequent heat release associated with ammonia dissolution in water. This competing thermal balance is expected to produce complex and rapidly evolving temperature profiles in both the water and air phases immediately downstream of the release point.

A detailed observation of the injection nozzle reveals a significant accumulation of frost on the injection pipe, indicating that the wall pipe temperatures well below 0°C due to the upstream expansion of the gas within the release pipe (Figure 34). This thermal gradient facilitates partial re-liquefaction within the piping. The presence of a distinct circular impact zone on the water surface confirms that the ammonia enters the basin partly in liquid form. This transition from a gaseous plume to localized liquid droplets is essential for the energy balance: it concentrates the exothermic dissolution reaction at the point of impact, potentially creating a sharp temperature contrast in the water between the extreme cold of the liquid ammonia (approximately -33°C) and the subsequent heat of reaction.

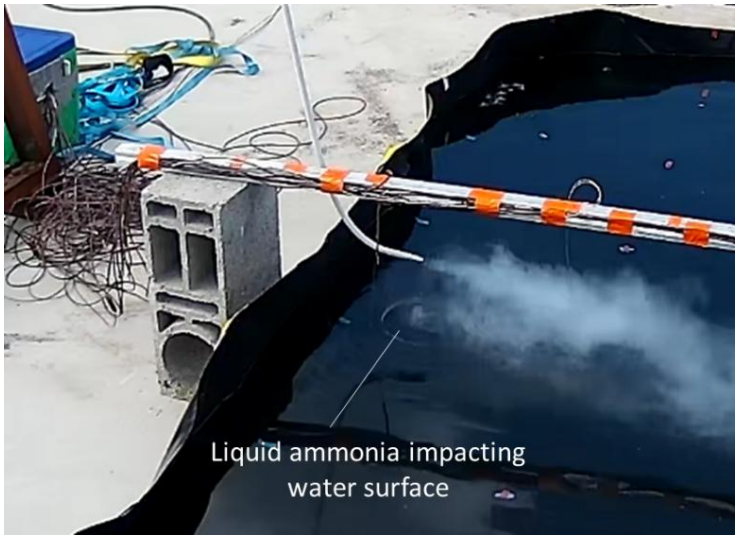

Figure 34: Close-up view of the ammonia injection nozzle during the release, showing frost accumulation on the supply pipe and a distinct liquid ammonia impact zone at the water surface, indicative of partial re-liquefaction of ammonia within the piping system prior to discharge.

The aerial thermal infrared image presented in Figure 35 provides a top-down view of the thermal footprint of the ammonia plume during the release. The dark region extending from the nozzle exit across the water surface corresponds to the cold thermal signature of the expansion-cooled ammonia aerosol, confirming that the plume remains concentrated at the water surface level and in direct contact with the pool along the entire length of the thermocouple array. The longitudinal extent of this cold signature is consistent with the sustained ground-hugging behaviour of the plume observed in the visible light images.

The propagation dynamics of the ammonia jet above the water surface can be described in terms of three successive regimes classically associated with the expansion of a

pressurized fluid. In the near-field region, the plume dynamics are dominated by the initial momentum of the jet at the nozzle exit, driving rapid forward propagation along the release axis. As the jet momentum dissipates with increasing distance from the nozzle, the plume transitions into a gravity-dominated regime, in which the negative buoyancy of the cold, dense ammonia aerosol becomes the controlling factor. The progressive widening of the cold infrared signature observed in Figure 35 , combined with the tendency of the plume to settle and remain near the water surface, is characteristic of this transition. In the far field, passive atmospheric dispersion is expected to govern the dilution and transport of the ammonia cloud. Under the experimental conditions tested, the thermal imagery and visible light camera recordings indicate that the plume dynamics above the water surface were primarily governed by the momentum-dominated and gravity-dominated regimes, with the cold dense aerosol remaining confined close to the water surface throughout the observation period.

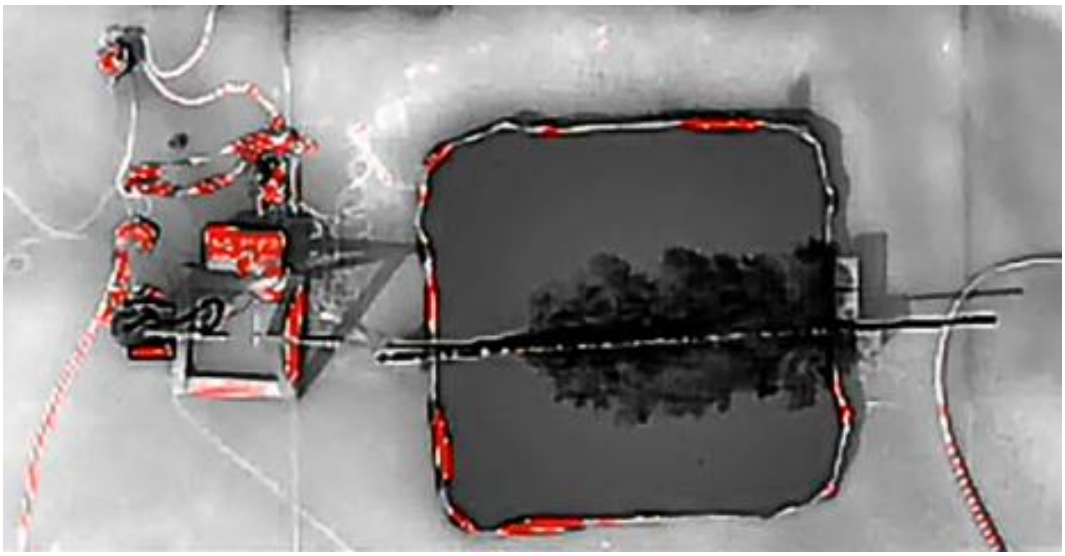

Figure 35: aerial thermal infrared image of the pressurized liquid ammonia release recorded by the SDIS 29 drone during the test. The dark region extending from the nozzle exit across the water surface represents the cold thermal signature of the expansion-cooled ammonia plume, confirming its ground-hugging behaviour and sustained contact with the water surface along the entire sensor array

Figure 36 presents simultaneous visible light and thermal infrared aerial images of the pool recorded after the ammonia release, providing complementary evidence of the chemical impact of the discharge on the water body. In the visible image, a diffuse white precipitate cloud is clearly visible at the water surface, consistent with the formation of ammonium hydroxide and associated reaction products upon dissolution of ammonia in seawater. The synchronized infrared image reveals a corresponding warm thermal signature in the same region, confirming that the exothermic dissolution reaction occurs rapidly at the air-water interface and generates a localized heat source within the pool despite the aerial mode of discharge.

The irregular and spatially extended shape of both the precipitate cloud and the thermal signature indicates that once the initial momentum of the jet has dissipated, the further transport and chemical impact of ammonia within the water body are governed by passive diffusion and convective mixing rather than by the directed dynamics of the release. This observation highlights the persistence of dissolved ammonia in the liquid phase well beyond the active injection period, with the pollutant continuing to spread laterally through the pool under the influence of slow water currents and concentration-driven diffusion. These post-release dynamics underscore the importance of considering not only the immediate impact zone but also the longer-term evolution of the dissolved ammonia plume when assessing the environmental and safety consequences of liquid ammonia spills onto water surfaces.

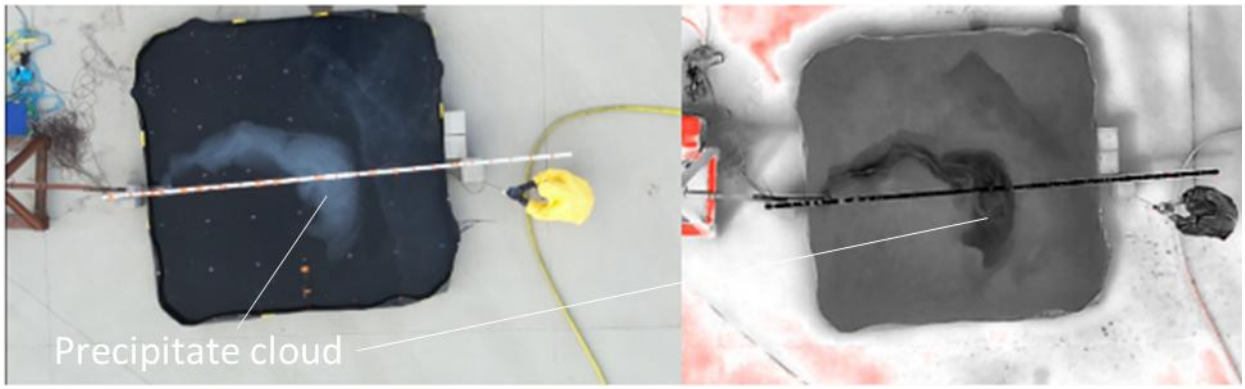

Figure 36: Simultaneous visible light (left) and thermal infrared (right) aerial images of the water pool recorded after the pressurized liquid ammonia release. The visible image reveals a white precipitate cloud at the water surface resulting from the exothermic dissolution of ammonia in seawater, while the infrared image shows the corresponding thermal signature, with warmer zones indicating localized heat release associated with the dissolution.

Figure 37 presents the air temperature time histories recorded during the pressurized liquid ammonia release, which lasted approximately 3 minutes. It should be noted that achieving a continuous and steady release was challenging during the test, as the supply pipe was subject to intermittent freezing caused by the adiabatic expansion of ammonia, temporarily blocking the flow. Sustained discharge could only be maintained by allowing periodic thermal recovery of the line, which accounts for the fluctuating temperature signal observed at T_air_1 throughout the injection period.

The reference sensor T_air_0, located 25 cm upstream of the release point, remained stable at approximately 23°C throughout the entire test, confirming that the ambient air temperature was unaffected by the release and providing a reliable thermal baseline. In contrast, T_air_1, positioned 5 cm downstream of the nozzle, recorded a minimum temperature of approximately −14°C, providing direct quantitative evidence of the intense adiabatic cooling induced by the expansion of pressurized liquid ammonia at the nozzle exit. This extreme near-field cooling is fully consistent with the frost accumulation observed on the supply pipe and the partial re-liquefaction of ammonia within the piping

system discussed previously. The synchronous temperature depression recorded across all downstream sensors (T_air_2 to T_air_5) during the injection period confirms that the cold ammonia aerosol plume successfully enveloped the entire thermocouple array, validating the alignment of the plume with the measurement axis.

Following the end of the injection at approximately t = 4 min, all sensors exhibited a rapid recovery toward ambient conditions, reflecting the efficient thermal equilibration of the cold aerosol plume through turbulent mixing with the warmer surrounding air. As the plume propagates downwind, the progressive entrainment of ambient air at 23°C raises the mixture temperature and dilutes the ammonia concentration, consistent with the transition from a momentum- and gravity-dominated regime to a passive dispersion regime observed in the thermal imagery. This rapid atmospheric warming confirms that the persistence of the cold aerosol is primarily limited to the active injection period, beyond which dilution and heat exchange with the environment quickly restore near-ambient conditions.

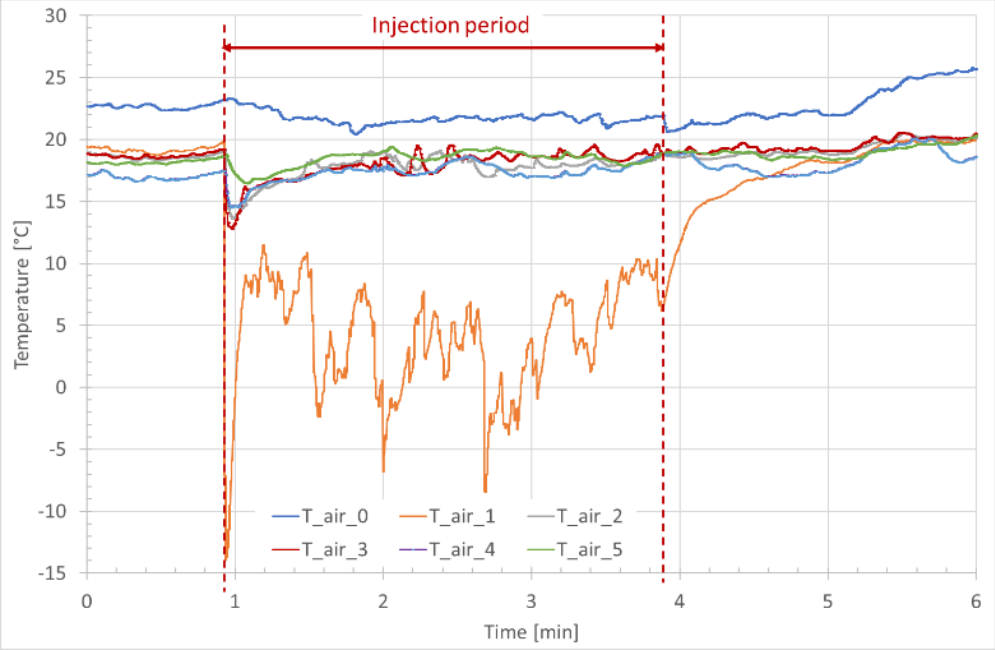

Figure 37: Temporal air temperature histories recorded by the six thermocouple sensors (T_air_0 to T_air_5) during the pressurized liquid ammonia release. The injection period (approximately t = 1 to t = 4 min) is indicated by the red dashed lines. T_air_0, located 25 cm upstream of the release point, serves as an ambient reference and remains stable at approximately 23°C throughout the test.

Figure 38 presents the water temperature time histories recorded at 5 cm below the water surface during the ammonia release. In sharp contrast to the pronounced thermal response observed in the air phase, all water temperature sensors remained within a narrow range of approximately 26.2°C to 26.8°C throughout the entire test, reflecting the high thermal inertia of the water body and its capacity to buffer local thermal perturbations.

A slight upward temperature trend was observed for sensors T_eau_1 to T_eau_4 during the injection period, which could be tentatively attributed to the local heat release associated with the exothermic dissolution of ammonia in seawater. However, these variations remain within the measurement uncertainty range of standard Type-T thermocouples (±0.5°C), making it difficult to unambiguously distinguish a genuine thermal signal from background noise or natural convection within the pool. Furthermore, analysis of the aerial imagery suggests that the sub-surface dissolution plume was not perfectly aligned with the thermocouple array, meaning that the water temperature sensors were likely positioned at the periphery rather than at the core of the exothermic reaction zone. This spatial offset would explain the limited thermal response recorded by the submerged sensors and underscores the complementary value of drone-based thermal infrared imaging for capturing the full spatial extent of the chemical impact within the basin, beyond what can be inferred from point measurements alone.

Sensor T_eau_5 (purple curve) exhibited an anomalous behaviour, displaying a lower baseline temperature and a slight downward trend throughout the test. This deviation is likely attributable to a positioning issue, whereby the sensor may have been partially exposed to the cold ammonia aerosol at the air-water interface, or to a localized cooling effect caused by the dense cold gas settling at the end of the pool and locally depressing the surface water temperature.

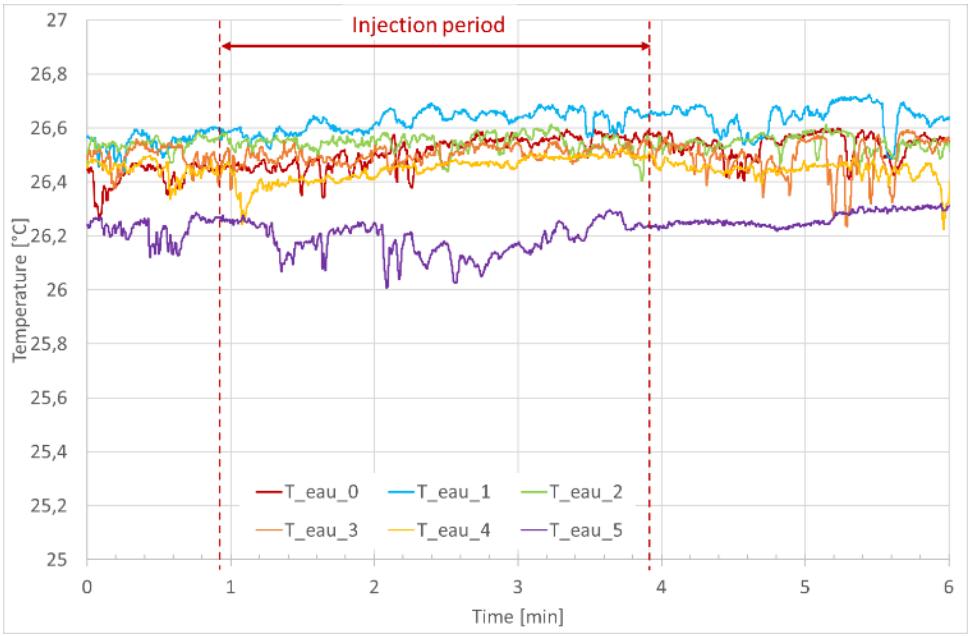

Figure 38: Temporal water temperature histories recorded by the six thermocouple sensors (T_eau_0 to T_eau_5) at 5 cm below the water surface during the pressurized liquid ammonia release. The injection period (approximately t = 1 to t = 4 min) is indicated by the red dashed lines.

Figure 39 presents the atmospheric ammonia concentrations recorded by two Dräger explosimeters positioned in the vicinity of the test area to assess potential exposure risks to operators. It should be noted that the upper measurement limit of the Dräger explosimeter is approximately 280 ppm, meaning that peak concentrations recorded at this value may reflect sensor saturation rather than the true atmospheric concentration, which could have been significantly higher during the most intense phases of the release. The primary sensor (blue markers) recorded peak concentrations reaching this upper limit, while the secondary sensor (orange markers) recorded a peak concentration of approximately 120 ppm. The pronounced temporal variability observed in both datasets is characteristic of turbulent passive dispersion of the gas cloud, consistent with the intermittent and structured plume dynamics observed in the thermal infrared imagery.

A notable feature of the atmospheric concentration data is the significant time lag observed between the onset of ammonia injection and the first detection of elevated concentrations by the sensors. This delayed response is consistent with the behaviour previously observed during the subsea ammonia injection experiments conducted at the CEDRE basin, where atmospheric concentration peaks were systematically recorded well after the end of the injection phases, confirming that volatilization from the water body rather than direct atmospheric release is the dominant source of prolonged atmospheric exposure.

Although the active injection phase lasted approximately 3 minutes, residual atmospheric ammonia concentrations of up to 50 ppm were detected well after the end of the release, with measurable concentrations persisting beyond t = 500 s. These post-injection detections are unlikely to originate from the initial gas cloud, which would have been rapidly diluted by atmospheric mixing following the cessation of the release. Instead, they are attributed to the volatilization of ammonia dissolved in the water body, which transitions from an active dissolution zone during the release to a secondary atmospheric emission source thereafter, sustaining a residual hazardous atmosphere through continuous air-water exchange driven by the concentration gradient between the ammonia-saturated water surface and the ambient air. This behaviour further highlights the persistent atmospheric hazard associated with ammonia spills onto water surfaces even after the active release has ceased, and underscores the importance of continued atmospheric monitoring well beyond the end of any ammonia discharge.

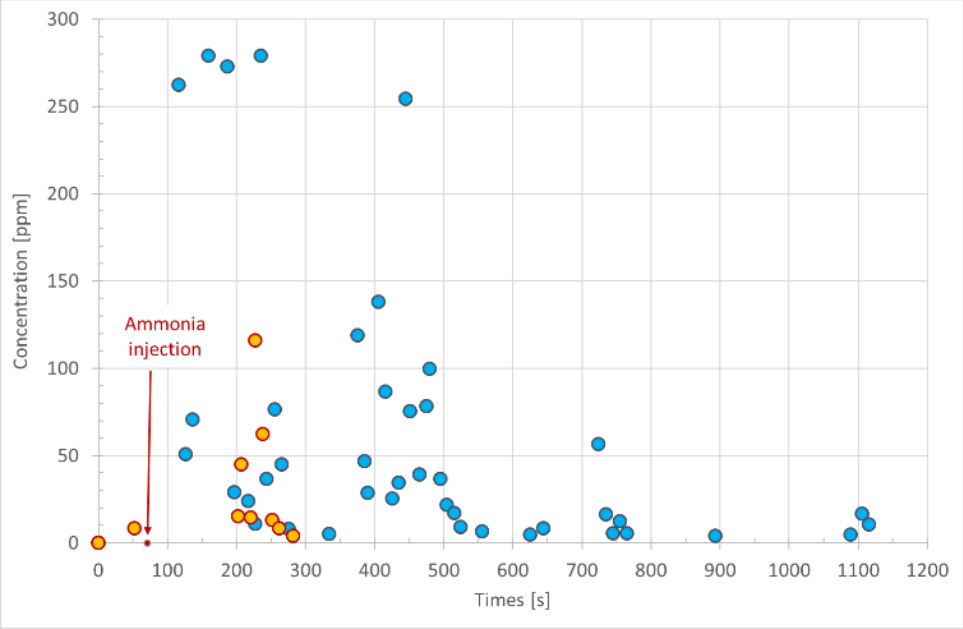

Figure 39: Atmospheric ammonia concentration measured by two Dräger explosimeters (blue and orange markers) in the vicinity of the test area during and after the pressurized liquid ammonia release. The onset of ammonia injection is indicated by the red arrow.

This experimental phase, conducted at the SDIS 29 training site, investigated the thermal, chemical and dispersive dynamics of a pressurized liquid ammonia release onto a water surface. The instrumentation comprised a network of 12 Type-T thermocouples deployed along the release axis to measure thermal gradients in both air and water, complemented by a WiMo probe for pH and temperature monitoring, an NH_4^+ ion-selective probe to quantify dissolved ammonium concentrations, and a comprehensive imaging suite including visible light surveillance cameras, a FLIR infrared camera with an ONERA ammonia-specific detector, and a SDIS 29 drone equipped with thermal imaging.

Visual observations confirmed that liquid ammonia exits the nozzle as a dense white two-phase plume, generated by the rapid adiabatic expansion of the pressurized fluid at the nozzle exit. This expansion induces intense cooling through the Joule-Thomson effect, evidenced by frost accumulation on the supply pipe and a minimum air temperature of approximately −14°C recorded at the nearest sensor. Although pure ammonia gas is lighter than air under ambient conditions, the cold moisture-laden aerosol formed at the nozzle exit is denser than the surrounding atmosphere, causing the plume to remain close to the water surface and maximizing contact time and physicochemical interactions at the air-water interface. Aerial thermal infrared imagery further confirmed this ground-hugging behavior, revealing a cold thermal signature extending along the entire thermocouple array, and showed that the plume dynamics transitioned rapidly from a momentum-dominated near-field regime to a gravity-dominated regime within a short distance from the nozzle.

The air temperature measurements confirmed the severe thermal impact of the release, with T_air_1 recording a minimum of approximately −14°C during the injection period and all downstream sensors (T_air_2 to T_air_5) exhibiting a synchronous thermal depression, validating the full lateral coverage of the sensor array by the cold ammonia plume. In contrast, the water temperature sensors remained within a narrow range of approximately 26.2°C to 26.8°C throughout the test, reflecting the high thermal inertia of the water body. The slight upward temperature trend observed in the near-field water sensors during injection may be tentatively attributed to the exothermic dissolution of ammonia in seawater, though these variations remained within the measurement uncertainty of the thermocouples. Post-release dual visible and infrared aerial imaging provided complementary confirmation of the exothermic dissolution reaction, revealing plumes of white precipitates at the water surface associated with residual warm thermal signatures in the basin, and indicating that the chemical impact continues to evolve after the active injection has ceased through passive diffusion and convective mixing within the water body.

Atmospheric concentration measurements recorded by the Dräger explosimeters — with an upper measurement limit of approximately 280 ppm — revealed peak concentrations reaching this saturation threshold during the active injection phase, indicating that actual concentrations may have been even higher. A significant time lag was observed between the onset of injection and the first atmospheric detections, consistent with the delayed volatilization behaviour previously identified during the subsea ammonia injection experiments at the CEDRE's basin. Furthermore, residual atmospheric concentrations of up to 50 ppm persisted well beyond the end of the injection phase, with detections recorded beyond t = 500 s. This prolonged atmospheric presence confirms that the water body transitions from an active dissolution zone during the release to a secondary emission source thereafter, sustaining a hazardous atmosphere through continuous volatilization driven by the concentration gradient at the air-water interface. These findings collectively underscore the complexity of the physicochemical processes governing liquid ammonia spills onto water surfaces and highlight the critical importance of sustained atmospheric monitoring well beyond the cessation of any ammonia discharge.

2.3.2. Cryogenic liquid release at sea surface

2.3.2.1. Experimental setup

The experiments were conducted outdoors in a portable water pool (Justrite Rigid-Lock QuickBerm®) with dimensions of 3 m × 3 m and a total height of 30 cm, filled with water to a depth of 19 cm. The pool was filled with water maintained at an initial temperature of approximately 22°C. Cryogenic liquid nitrogen was stored in an open-top cryogenic vessel and released onto the water surface by tilting the vessel using a wire-and-pulley

system mounted on a rigid frame positioned at one end of the pool. This release mechanism ensured a repeatable and controlled spill initiation, as illustrated in Figure X. Four successive release tests were performed, with liquid nitrogen masses of 3, 5, 7 and 12 kg respectively, in order to investigate the influence of the released mass on the thermal and dispersive behaviour of the cryogenic spill.

Temperature measurements were performed using a network of Type-T thermocouples arranged along the central axis of the pool, aligned with the release axis. Sensors were placed at six positions located at 20, 60, 120, 220, 280 and 340 cm from the release point, so as to capture the thermal attenuation of the cryogenic cloud as it propagates downrange. At each position, two sensors were deployed simultaneously: one in air, placed 15 cm above the water surface, and one in water, placed 5 cm below the water surface. All temperature signals were acquired at a sampling frequency of 10 Hz using a data acquisition system. Type-T thermocouples were selected for their accuracy in the low-temperature range, which is particularly suited to cryogenic applications.

In addition to the thermocouple network, the experiment was instrumented with three imaging systems providing complementary perspectives on the phenomenon. A visible light camera recorded the temporal evolution of the vapor cloud from a lateral viewpoint, enabling detailed visualization of the cloud propagation dynamics along the release axis. A drone was deployed above the pool to provide a top-down aerial view of the nitrogen spill, allowing the lateral spreading of the cloud over the water surface to be characterized. Finally, a FLIR SC6700 infrared camera was positioned to monitor the thermal footprint of the nitrogen release on the water surface. Together, these measurement systems provided both quantitative thermal data and qualitative visual information on the cryogenic spill phenomenon.

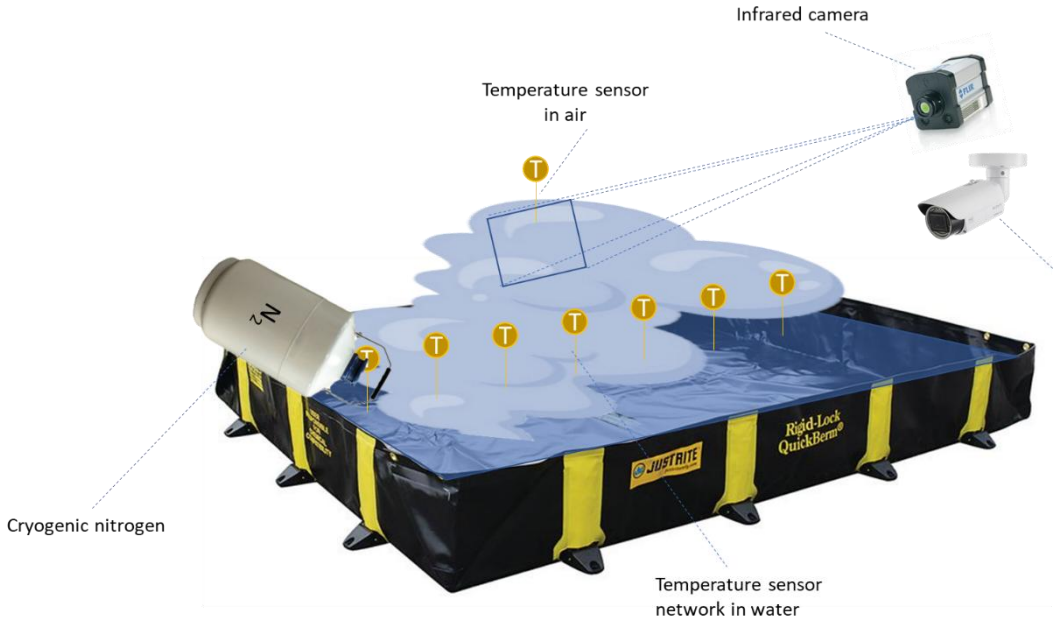

Figure 40: Schematic overview of the experimental setup. Cryogenic liquid nitrogen is released from an open-top vessel onto the water surface of a 3 m × 3 m portable pool. Temperature measurements are performed by a network of Type-T thermocouples deployed along the release. The experiment is monitored by a visible light camera and a FLIR SC6700 infrared camera

Figure 41: Temporal Photograph of the experimental setup prior to the cryogenic nitrogen release. The portable water pool is filled with seawater. The open-top cryogenic nitrogen vessel is visible in its initial tilted position at the edge of the pool, held by the wire-and-pulley release mechanism. The thermocouple support rail is mounted along the central axis of the pool.

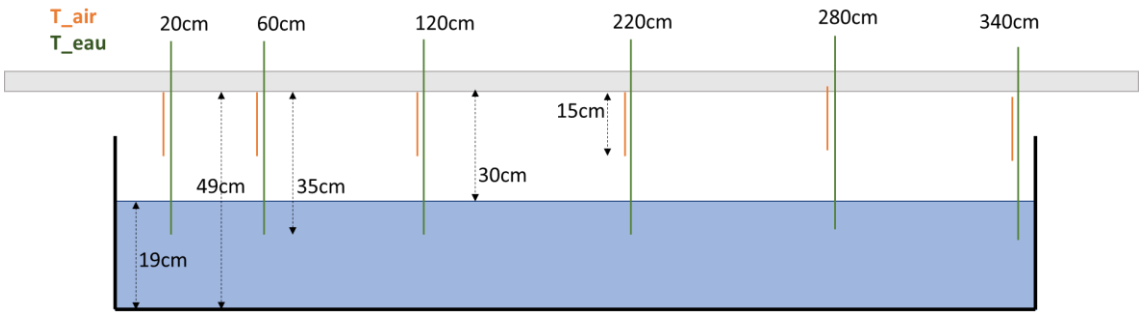

Figure 42: Schematic side view of the thermocouple array deployment along the central axis of the pool. Air temperature sensors (T_air, orange) are positioned 15 cm above the water surface, and water temperature sensors (T_eau, green) are placed 5 cm below the water surface, at six measurement positions located at 20, 60, 120, 220, 280 and 340 cm from the release point. The water depth is 19 cm and the total pool height is 30 cm.

2.3.2.2. Analysis of experimental results

- **Visual observation**

The sequential images recorded during the experiment reveal the rapid propagation of the cold vapor cloud generated upon the release of cryogenic nitrogen onto the water surface. At t_0 = 0.00 s, the water surface remains undisturbed, with no visible cloud present. As early as t_1 = 0.40 s, a white vapor cloud begins to form at the release point. The white appearance of the cloud is characteristic of the condensation of atmospheric water vapor, which occurs as the surrounding humid air is rapidly cooled below its dew point by contact with the cryogenic nitrogen and its cold evaporation products. This condensation phenomenon is thus an indirect tracer of the cold gas dispersion rather than a direct visualization of the nitrogen itself.

The cloud expands rapidly and progressively covers the entire pool surface, reaching the far end of the basin by t_5 = 2.00 s, corresponding to a propagation distance of approximately 250 cm in less than 2 seconds. The propagation dynamics are governed by the interplay of several physical mechanisms. First, the initial momentum of the cryogenic release imparts a preferential direction to the cloud, driving it along the release axis. Second, the evaporation kinetics of liquid nitrogen — which vaporizes almost instantaneously upon contact with the warmer water surface due to the large temperature difference — generates a rapid and sustained volumetric expansion of cold gas, further fuelling the cloud growth. Third, ambient wind conditions present during the outdoor experiment likely contributed to the directionality and asymmetry of the cloud dispersion, advecting the vapor preferentially downwind.

Throughout the sequence, the cloud grows in both height and lateral extent, overflowing beyond the pool boundaries, which suggests that the cold dense gas

spreads not only along the water surface but also rises and disperses into the surrounding atmosphere as it warms and its density approaches that of ambient air.

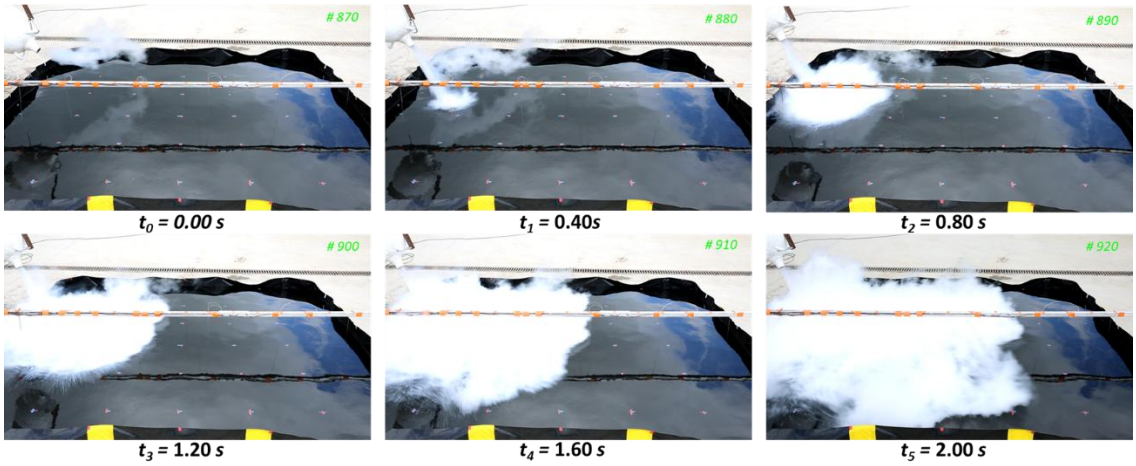

Figure 43: Lateral time-lapse sequence of the cold vapor cloud propagation following a cryogenic nitrogen release onto the water surface. Images are captured at t_0 = 0.00 s (prior to release), t_1 = 0.40 s, t_2 = 0.80 s, t_3 = 1.20 s, t_4 = 1.60 s and t_5 = 2.00 s. The white cloud, resulting from the condensation of atmospheric water vapor in the cold nitrogen gas layer, propagates rapidly along the release axis and covers the entire pool surface within 2 seconds, overflowing beyond the pool boundaries.

- **Air temperature measurements**

The air temperature sensors, positioned 15 cm above the water surface along the release axis, recorded sharp and spatially dependent thermal depressions following each cryogenic nitrogen release. Prior to each test, all sensors indicated stable ambient air temperatures of approximately 20–22°C. In all four tests, the onset of the temperature drop was nearly simultaneous across the sensor array, consistent with the rapid propagation of the cold vapor cloud observed visually. Following the thermal minimum, all sensors exhibited a gradual recovery toward ambient conditions, typically within 3 to 5 minutes after the release, reflecting the progressive warming and dilution of the cold gas layer by the surrounding atmosphere.

Across all four tests, a consistent spatial pattern was observed: the magnitude of the temperature depression generally decreased with increasing distance from the release point, with the nearest sensor T_air_1 systematically recording among the lowest temperatures. A clear influence of the released mass on the overall severity of the thermal response was also observed, with larger releases producing deeper and more spatially extensive temperature drops. However, this trend was not strictly monotonic for all sensors across all tests, likely reflecting the influence of varying ambient wind conditions between tests, which may have altered the directionality and dilution rate of the cold cloud. Notably, during the 7 kg release, T_air_2 recorded an anomalously low minimum of approximately 3°C compared to sensors at similar or greater distances, a

behaviour likely attributable to direct contact between a liquid nitrogen droplet and the thermocouple junction rather than the actual local gas temperature.

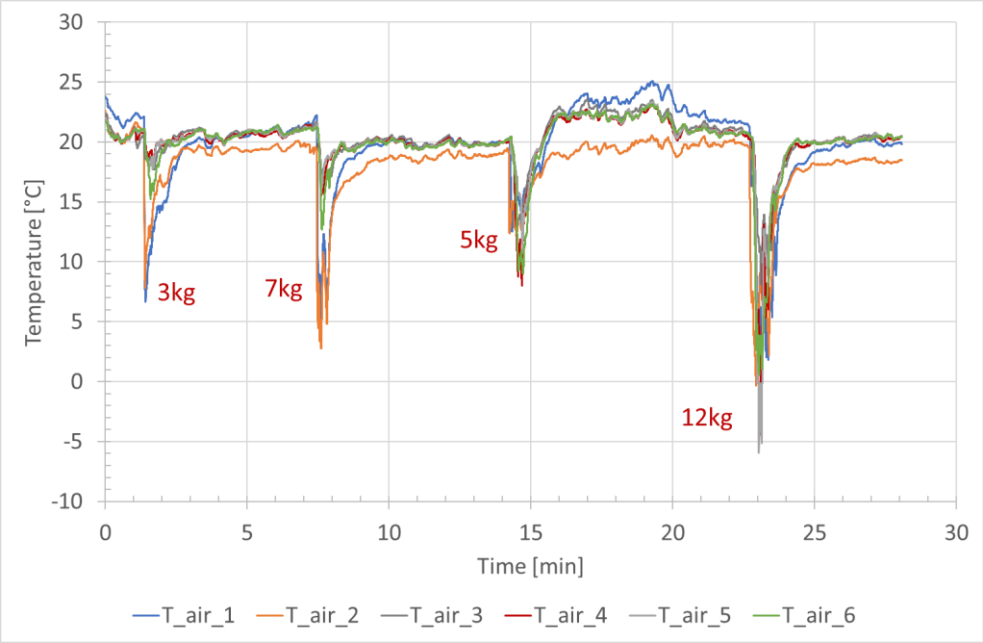

Figure 44: Air temperature time histories recorded by the six thermocouple sensors during the four successive cryogenic nitrogen release tests (3, 7, 5 and 12 kg). Each release produces a sharp and transient temperature depression, the magnitude and spatial extent of which increases with the released mass.

- **Focus on the 12 kg release — air temperatures**

The 12 kg release produced the most severe and spatially extensive thermal decrease of the entire test campaign, with all six air temperature sensors recording significant cooling. Prior to the release, ambient air temperatures were stable at approximately 20–21°C across all measurement points. The thermal event initiated abruptly at approximately t = 2.7 min, with a quasi-simultaneous temperature drop recorded across the entire sensor array, indicating that the cold vapor cloud propagated rapidly and reached all measurement positions within a very short time interval.

The minimum temperatures recorded at each sensor position reveal a complex spatial pattern. T_air_1, located at 20 cm from the release point, reached a minimum of approximately 2°C, corresponding to a drop of nearly 21°C from its initial value. T_air_2, at 60 cm, dropped to approximately 0°C and exhibited the slowest thermal recovery of all sensors, remaining several degrees below ambient temperature for several minutes after the event. Unexpectedly, the lowest temperature of the entire campaign was recorded not at the nearest sensor but at T_air_5, located at 280 cm from the release point, which reached a minimum of approximately −6°C. Similarly, T_air_6 at 340 cm

recorded a minimum of approximately 1°C, lower than T_air_3 and T_air_4 located at 120 and 220 cm respectively, which reached minima of approximately 13°C and 7°C. This non-monotonic spatial distribution of minimum temperatures suggests that the cold cloud dispersion was influenced by ambient conditions during the test, which may have advected the densest and coldest portion of the cloud preferentially toward the distant sensors rather than following a simple axisymmetric dilution pattern.

The overall duration of the significant thermal depression, defined as the period during which at least one sensor recorded a temperature below 10°C, was approximately 1.5 minutes, between t ≈ 2.7 min and t ≈ 4.2 min. Following the minimum, all sensors exhibited a progressive recovery toward ambient conditions, with most returning to near-initial values within approximately 3 to 4 minutes after the onset of the event. T_air_2 was the notable exception, remaining persistently below ambient temperature throughout the observation period, which may reflect a more sustained local cooling effect at close range to the release point, consistent with the prolonged presence of evaporating liquid nitrogen in the near-field region.

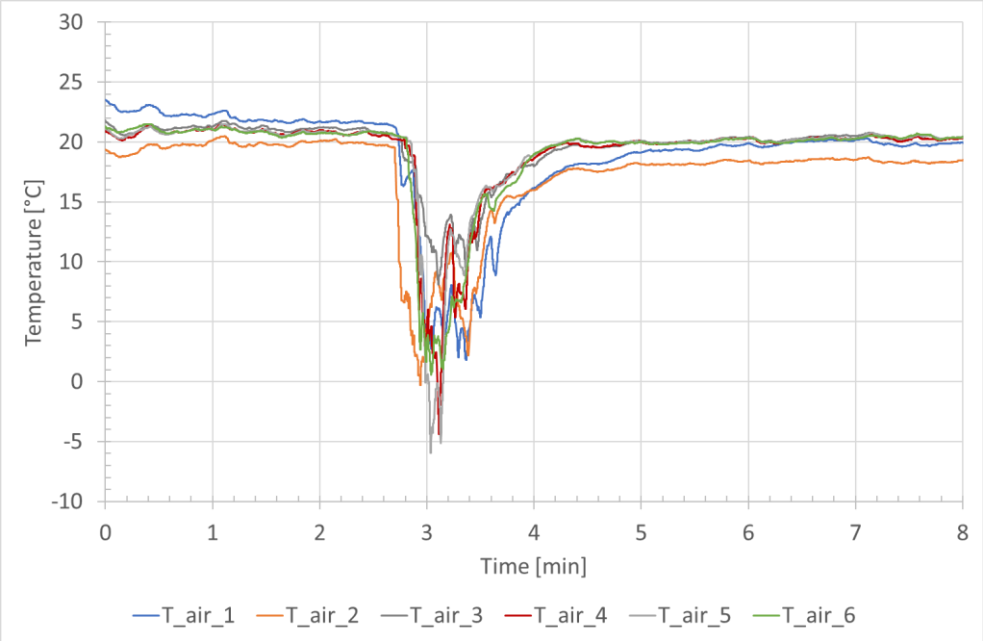

Figure 45: Temporal air temperature recorded by the six thermocouple sensors during the 12 kg cryogenic nitrogen release.

The recorded minimum temperatures, while reflecting significant thermal release, remain considerably higher than the boiling point of liquid nitrogen (−196°C). This observation is physically consistent and can be attributed to several concurrent mechanisms. First, liquid nitrogen vaporizes almost instantaneously upon contact with the water surface due to the large temperature difference between the two fluids, and the resulting cold nitrogen gas rapidly mixes with the warmer ambient air, leading to significant thermal dilution before reaching the sensors. Second, the turbulent mixing

induced by the momentum of the release further accelerates this dilution process. Third, the sensors are located 15 cm above the water surface, whereas the coldest gas layer, being denser than ambient air, tends to remain close to the water surface, meaning the sensors may not capture the absolute minimum temperatures occurring at the air-water interface.

A notable physical phenomenon observed during the experiments was the Leidenfrost effect at the water surface. Patches of liquid nitrogen were seen moving erratically across the water surface, exhibiting a characteristic levitation behaviour in which the nitrogen pools glided freely without immediately vaporizing [4], [5]. This effect occurs when the water surface temperature is sufficiently high relative to the boiling point of nitrogen, causing the formation of an insulating vapor film beneath the liquid nitrogen layer that thermally decouples it from the water surface and significantly slows down the evaporation rate (Figure 46). This delayed evaporation prolongs the presence of liquid nitrogen at the surface and contributes to sustaining the cold gas source over a longer duration than would be expected from simple contact vaporization.

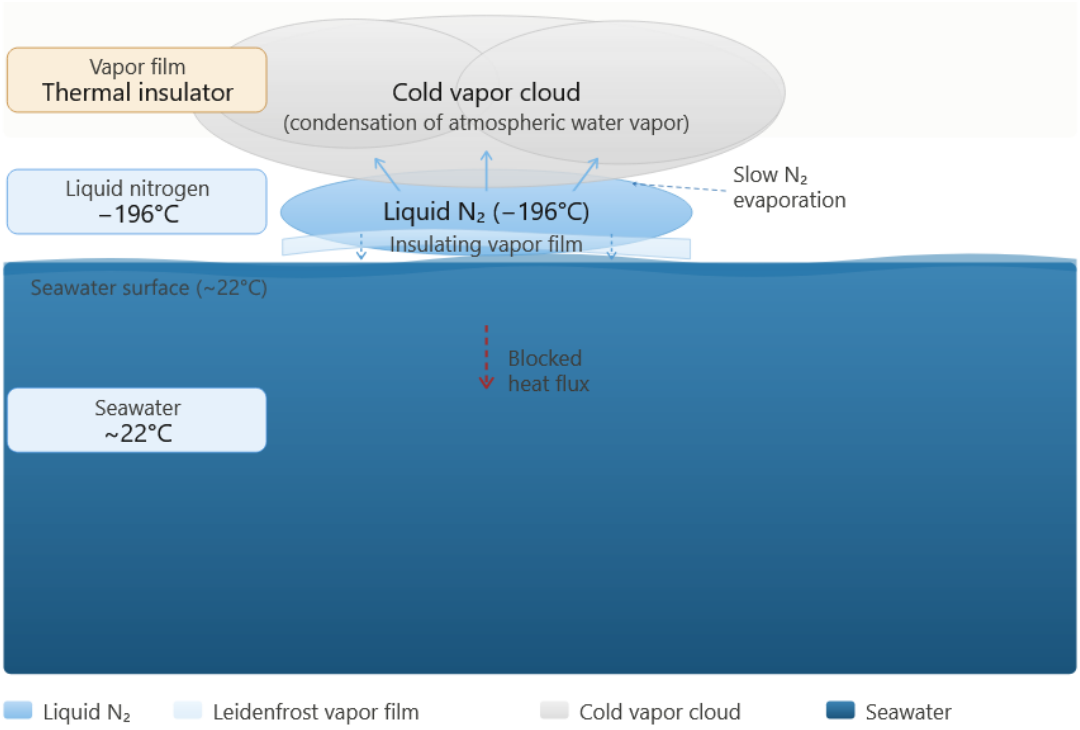

Figure 46: Schematic illustration of the Leidenfrost effect during cryogenic liquid nitrogen spill onto a seawater surface. The insulating vapor film formed beneath the liquid nitrogen patches (−196°C) thermally decouples the cryogenic liquid from the water body, significantly reducing heat transfer and sustaining the cold gas source over the pool surface

- **Water measurements**

The water temperature sensors, placed 5 cm below the water surface along the release axis, recorded only marginal temperature variations throughout the entire test campaign, in sharp contrast to the pronounced thermal depressions observed in the air. Prior to each release, all sensors indicated stable water temperatures in the range of 21.7°C to 22.2°C. Following each cryogenic nitrogen release, the water temperature fluctuations remained extremely limited, with maximum deviations of approximately 1 to 2°C from the initial values, even for the largest 12 kg release. This is particularly striking given the severity of the thermal response recorded simultaneously in the air phase.

Across all four tests, no clear spatial pattern was observed in the water temperature response: the sensors closest to the release point were not systematically the most affected, and the magnitude of the fluctuations did not increase monotonically with the released mass. This contrasts with the spatially organized thermal response observed in the air and suggests that the water temperature variations are not driven by a sustained and directional heat extraction process, but rather by localized and transient phenomena. Two physical mechanisms are believed to contribute to these fluctuations. First, the erratic displacement of liquid nitrogen spill at the water surface in the Leidenfrost regime may induce localized and intermittent heat extraction at the air-water interface, generating small thermal disturbances that propagate downward into the water column and are detected by the submerged sensors as brief temperature drops. Second, the violent vaporization of nitrogen at the water surface may induce localized convective mixing within the water body, momentarily bringing slightly cooler near-surface water into contact with the sensors.

The limited overall thermal response of the water can furthermore be explained by two complementary mechanisms. On one hand, the Leidenfrost effect thermally decouples the cryogenic liquid from the water surface by forming an insulating vapor film beneath the liquid nitrogen patches, thereby significantly reducing the net heat flux extracted from the water body. On the other hand, even in the absence of this insulating effect, the sensors located 5 cm below the water surface would be expected to respond only weakly and with a significant time delay, as any surface cooling would need to propagate downward through the water column by conduction and convection before being detected. The combination of these effects — reduced surface heat extraction due to the Leidenfrost regime, thermal inertia of the water column, and the absence of a sustained directional cooling source — thus provides a consistent physical explanation for the negligible temperature variations recorded by the submerged sensors throughout the experiment.

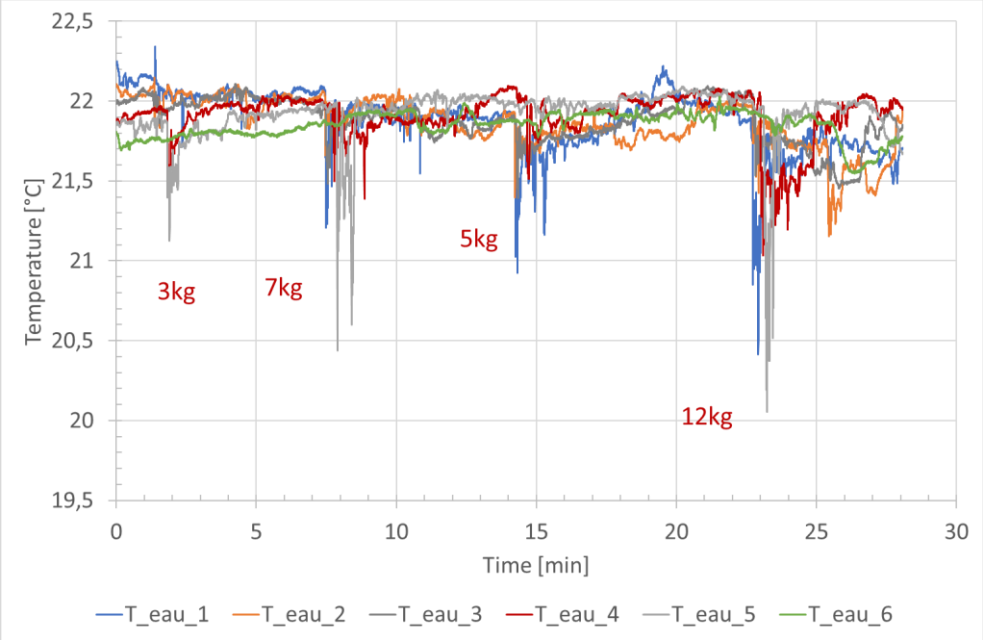

Figure 47: Temporal water temperature histories recorded by the six thermocouple sensors during the four successive cryogenic nitrogen release tests (3, 7, 5 and 12 kg). In contrast to the air temperature measurements, all sensors remain within a narrow temperature range of approximately 20.0°C to 22.3°C throughout the entire test campaign, with maximum deviations not exceeding 2°C from initial values.

- **Focus on the 12 kg release — water temperatures**

The zoomed water temperature data for the 12 kg release provides a more detailed picture of the thermal response within the water body. Prior to the release, all sensors indicated stable temperatures between 21.8°C and 22.1°C. The thermal event initiated at approximately t = 2.8 min, coinciding with the onset of the air temperature depression, and was characterized by a series of brief but pronounced temperature drops superimposed on a more gradual overall cooling trend.

The most significant response was recorded by T_eau_3, located at 120 cm from the release point, which reached an absolute minimum of approximately 20.1°C, representing a drop of nearly 2°C from its initial value. This sensor also exhibited multiple successive sharp temperature spikes, suggestive of repeated intermittent contact with cold water masses driven by the erratic displacement of liquid nitrogen patches in the Leidenfrost regime at the water surface above. T_eau_1, at 20 cm, dropped to approximately 20.4°C with a similarly brief and sharp profile, while T_eau_4 at 220 cm exhibited more moderate and sustained fluctuations of approximately 0.8°C persisting until t ≈ 4.5 min. In contrast, T_eau_5 and T_eau_6, located at 280 and 340 cm respectively, remained largely unaffected, with variations below 0.3°C throughout the event.

Notably, T_eau_2 displayed a delayed thermal response, with its most pronounced fluctuations occurring around t ≈ 5.5 min, well after the main thermal event had subsided for most other sensors. This delayed response is consistent with the slow lateral drift of liquid nitrogen patches across the water surface in the Leidenfrost regime, which may have reached the vicinity of this sensor at a later stage, locally enhancing the heat extraction from the water surface and generating a cold perturbation detectable at 5 cm depth.

Overall, the water temperature variations recorded during the 12 kg release, while more pronounced than for the smaller releases, remained limited to a maximum of approximately 2°C. This confirms that the thermal impact of the cryogenic nitrogen spill on the water body is substantially attenuated by the combined effects of the Leidenfrost insulating vapor film and the thermal inertia of the water column, with the liquid nitrogen patches acting as transient and localized rather than sustained heat sinks.

- **Thermal imaging**

The FLIR SC6700 infrared camera provided complementary qualitative observations of the thermal footprint of the cryogenic nitrogen release on and above the water surface. In the absence of any release, the infrared images showed a relatively uniform thermal signature across the water surface, consistent with the stable initial water temperature of approximately 22°C recorded by the submerged sensors. Following the nitrogen release, the infrared images revealed a strongly heterogeneous thermal field, with the cold vapor cloud appearing as a distinct region of contrasting thermal signature propagating across the water surface from the release point. The spatial extent and progression of this cold region are consistent with the rapid cloud propagation observed in the visible light images and with the thermal depressions recorded by the air temperature sensors. However, due to the highly transient and optically complex nature of the phenomenon — in particular the presence of a dense condensation cloud that partially obstructs the infrared signal — a fully quantitative analysis of the infrared data was not performed, and the infrared imagery is used here solely as a qualitative indicator of the spatial dynamics of the thermal event.

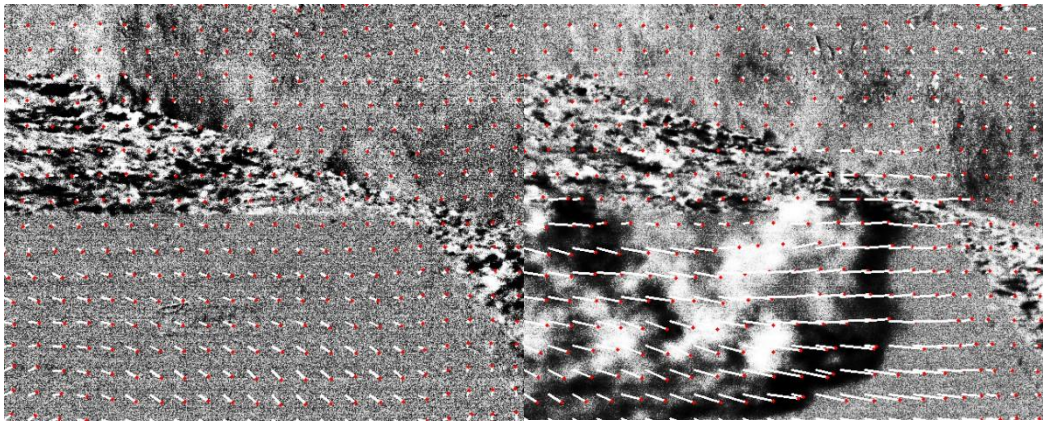

Figure 48: Infrared images of the water pool recorded by the FLIR SC6700 camera before (left) and during (right) the cryogenic nitrogen release. The pre-release image shows a relatively uniform thermal signature across the water surface, while the image recorded during the release reveals a strongly heterogeneous thermal field associated with the propagation of the cold vapor cloud and the presence of liquid nitrogen patches at the water surface.

The aerial drone imagery provided a particularly valuable top-down perspective of the cryogenic spill phenomenon, capturing both the early-stage liquid nitrogen behavior at the water surface and the full-scale vapor cloud propagation. During the initial phase of the release, drone images clearly revealed the presence of numerous discrete liquid nitrogen patches scattered across the water surface in the Leidenfrost regime, appearing as elongated bright streaks moving erratically across the pool, driven by the insulating vapor film beneath each patch. Their non-uniform distribution across the full pool extent, well beyond the release point, is consistent with the non-monotonic temperature responses observed along the sensor array.

As the release progressed, the nine-image drone sequence captured the complete temporal evolution of the cold vapor cloud from initiation to maximum dispersion. Starting from a localized white plume at the release point, the cloud expanded rapidly both vertically and laterally within the first few seconds, quickly covering the entire pool surface before propagating well beyond the pool boundaries. The cloud dispersion was clearly asymmetric and strongly directional, with ambient wind playing a dominant role in advecting the cold dense gas preferentially downwind. Due to its higher density relative to ambient air, the cold nitrogen gas remained close to the ground surface as it propagated beyond the pool, forming a dense ground-hugging layer that spread over a surface area estimated to be approximately five to ten times larger than the pool itself at maximum extent. The cloud remained dense and optically opaque throughout the sequence, indicating sustained nitrogen evaporation over the duration of the event. This extended ground-level propagation beyond the source area underscores the significant hazard zone potentially associated with large cryogenic spills in outdoor environments, where the cold asphyxiating gas cloud can reach distances well beyond the immediate spill area.

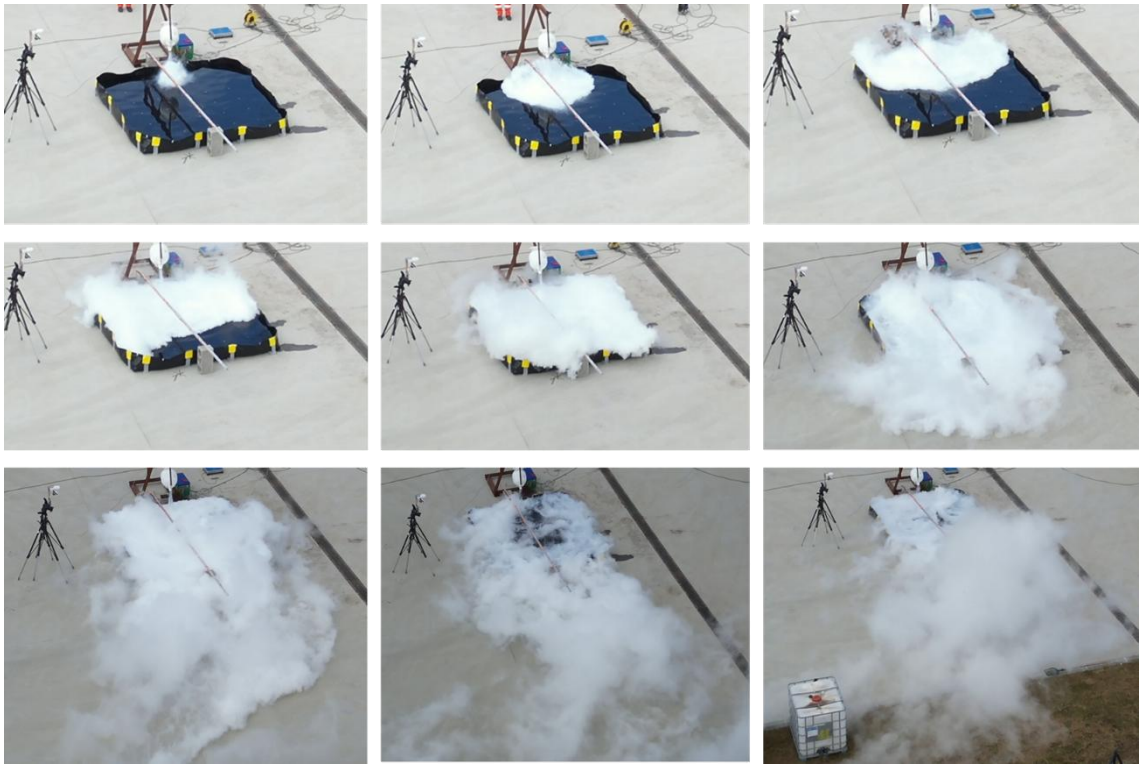

Figure 49: Aerial drone image sequence showing the temporal evolution of the cold vapor cloud during the 12 kg cryogenic nitrogen release, from initiation to maximum dispersion (left to right, top to bottom). The cloud forms rapidly at the release point and expands both vertically and laterally, quickly covering the entire pool surface before propagating well beyond the pool boundaries in the downwind direction. The cold nitrogen gas, denser than ambient air, forms a dense ground-hugging layer that spreads over a surface area significantly larger than the pool itself at maximum extent. The cloud remains dense and optically opaque throughout the sequence, reflecting sustained nitrogen evaporation over the duration of the event.

The aerial drone imagery provided a particularly striking top-down perspective of the cryogenic spill phenomenon. As illustrated in Figure X, the drone images clearly reveal the presence of numerous discrete liquid nitrogen patches scattered across the entire water surface, characteristic of the Leidenfrost regime. These patches appear as elongated bright streaks of varying size and orientation, their directional shape being indicative of rapid lateral motion across the water surface. Their distribution is non-uniform, with patches observed across the full extent of the pool, well beyond the release point, and their trajectories appear influenced by ambient wind conditions, with a preferential displacement toward the distal end of the basin. Between the patches, the dark water surface remains clearly visible, confirming that the liquid nitrogen contact with the water is intermittent and spatially localized rather than forming a continuous film. Small wisps of white vapor rising from the pool edges further confirm the active evaporation of nitrogen occurring at the periphery of each patch. This confirms the erratic and unpredictable nature of the liquid nitrogen displacement at the

water surface, driven by the insulating vapor film beneath each patch that effectively eliminates friction with the underlying water. The spatial distribution of these drifting patches, as captured by the drone, is fully consistent with the non-monotonic water and air temperature responses observed along the sensor array, as they locally sustain cold gas emission at unpredictable locations across the pool surface.

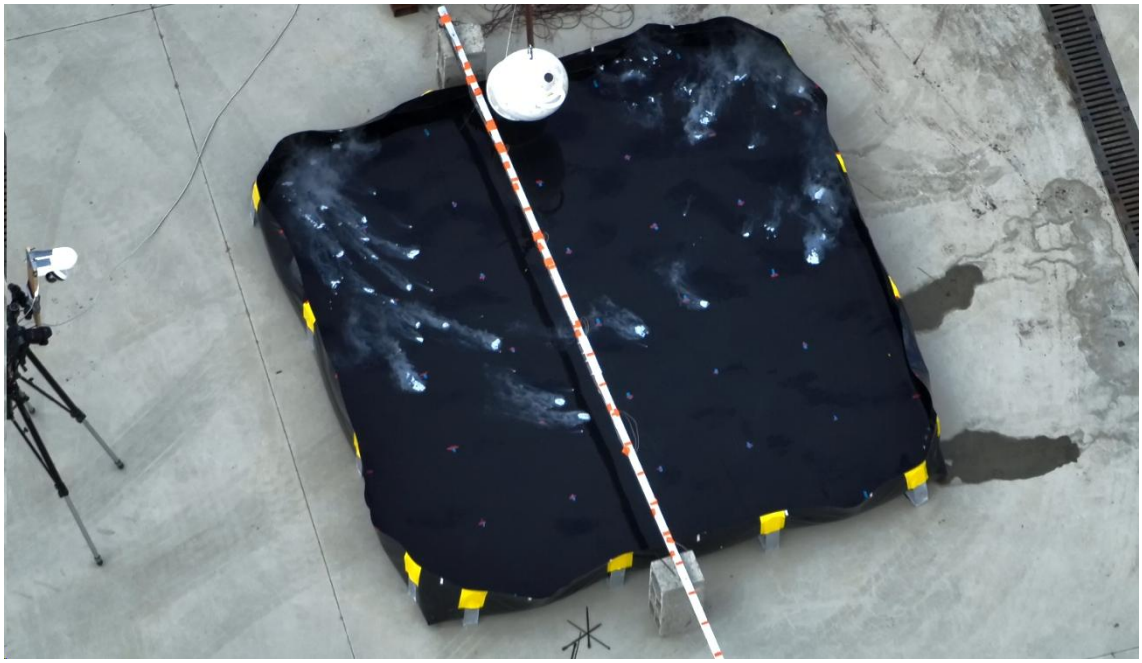

Figure 50: Top-down drone image of the water pool surface during a cryogenic nitrogen release, illustrating the Leidenfrost effect. Discrete liquid nitrogen patches are clearly visible as elongated bright streaks dispersed across the entire pool surface, well beyond the release point located at the top of the image. Their elongated and directional shape is indicative of rapid lateral motion driven by the insulating vapor film beneath each patch, which eliminates friction with the underlying water surface. Small wisps of vapor rising at the periphery of the patches confirm active nitrogen evaporation.

This chapter presented an experimental investigation of the thermal and dispersive behaviour of cryogenic liquid nitrogen released onto a water surface. Four release tests were conducted with increasing nitrogen masses (3, 5, 7 and 12 kg) in a 3 m × 3 m outdoor water pool filled with seawater, instrumented with a network of Type-T thermocouples in air and water, complemented by visible light, infrared and aerial drone imaging systems.

The visual observations revealed the extremely rapid propagation of a dense white vapor cloud, generated by the condensation of atmospheric water vapor in the cold nitrogen gas layer, covering the entire pool surface within 2 seconds and overflowing well beyond the pool boundaries. The cloud dynamics were governed by the initial momentum of the release, the evaporation kinetics of liquid nitrogen, and ambient wind conditions.

The air temperature measurements confirmed a sharp and transient thermal decrease following each release, with minimum temperatures decreasing with distance from the release point and increasing severity with released mass. The most extreme thermal event was recorded during the 12 kg release, with a minimum temperature of −6°C at 280 cm from the release point. The spatial distribution of minimum temperatures was non-monotonic, reflecting the combined influence of ambient wind and the erratic displacement of liquid nitrogen spills due to the Leidenfrost regime. Despite the large temperature drops recorded, all minimum values remained well above the boiling point of liquid nitrogen (−196°C), consistent with the rapid dilution and mixing of the cold gas with ambient air.

In contrast, the water temperature sensors recorded only marginal variations of 1 to 2°C throughout the entire test campaign, even for the largest release. This limited thermal response is attributed to the thermal insulation provided by the Leidenfrost vapor film at the water-nitrogen interface, which significantly reduces heat transfer from the water to the cryogenic liquid, combined with the thermal inertia of the water column that attenuates any surface cooling before it reaches the submerged sensors.

Finally, the infrared and drone imagery provided qualitative confirmation of the Leidenfrost regime, with liquid nitrogen patches clearly visible as elongated bright streaks drifting erratically across the pool surface, and of the large-scale ground-hugging vapor cloud propagating well beyond the pool boundaries, highlighting the significant spatial extent of the potential hazard zone associated with large cryogenic spills in outdoor environments.

3. Conclusion

This report presented the results of three complementary experimental campaigns investigating the behaviour of hazardous gas and liquid releases in and above water, covering a range of substances — methane, ammonia, and cryogenic nitrogen — and release configurations, from water subsurface gas injection above the water surface liquid spills.

The water subsurface methane injection experiments demonstrated that the hydrodynamic response of the free surface is governed by buoyancy-driven plume dynamics, with a free-surface elevation following a quasi-linear dependence on flow rate consistent with a confinement-controlled accumulation regime, and a swell propagation velocity well described by classical turbulent plume scaling laws. Atmospheric dispersion of methane above the surface was found to be highly intermittent and strongly influenced by ambient wind, highlighting the limitations of steady-state Gaussian dispersion assumptions in near-field configurations.

The subsurface ammonia injection experiments revealed a fundamentally different behaviour compared to methane, driven by the high solubility and reactivity of ammonia in seawater. Despite producing no visible surface disturbance, the ammonia releases generated significant chemical impacts on the water body, with seawater pH rising from 8.6 to 9.3 and atmospheric concentrations approaching the IDLH threshold of 300 ppm at only 30 cm above the surface. A notable visual indicator of the ammonia-seawater reaction was the formation of a white precipitate in the water column, resulting from the chemical interaction between dissolved ammonia and seawater constituents. This precipitate was clearly identified during the July 2025 tests and constitutes a useful qualitative indicator of active ammonia dissolution in the water body. Critically, both the pH elevation and the atmospheric concentration peaks were observed with time delays relative to the end of injection, confirming that volatilization of dissolved ammonia from the water body constitutes a persistent secondary emission source well after the active release has ceased. The identification of a critical pH threshold of approximately 8.8 beyond which volatilization becomes significant provides a potentially valuable early warning indicator for operational safety protocols.

The pressurized liquid ammonia surface release experiments further highlighted the complexity of ammonia spill dynamics. The adiabatic expansion of the pressurized fluid at the nozzle exit generated a cold, dense two-phase aerosol that remained close to the water surface, maximizing air-water contact and dissolution. Extreme near-field cooling of approximately −14°C was recorded immediately downstream of the nozzle, while the water body remained largely unaffected due to its high thermal inertia. Post-release dual visible and infrared imaging confirmed the persistence of the exothermic dissolution reaction through white precipitate formation and residual thermal signatures, and atmospheric monitoring revealed peak concentrations reaching the sensor saturation limit of 280 ppm with significant post-injection persistence, consistent with the volatilization mechanism identified in the subsurface injection experiments.

The cryogenic liquid nitrogen surface release experiments demonstrated the extremely rapid and dynamic nature of cryogenic spills onto water. The cold vapor cloud covered the entire pool surface within 2 seconds and propagated well beyond the pool boundaries, driven by the combined effects of release momentum, evaporation kinetics, and ambient wind. The Leidenfrost effect played a central role in governing both the evaporation dynamics and the thermal response of the water body, with erratically drifting liquid nitrogen patches sustaining localized cold gas emission at unpredictable locations across the pool and contributing to the non-monotonic spatial distribution of temperature minima observed along the sensor array. Despite temperature drops of up to 27°C in the air phase, the water body remained thermally stable, confirming the insulating role of the Leidenfrost vapor film.

Across all three experimental configurations, several recurring themes emerge. First, the coupling between underwater or water surface release dynamics and atmospheric dispersion is consistently governed by transient and highly intermittent processes that

cannot be adequately captured by steady-state models. Second, the water body systematically acts as a buffer for thermal perturbations while simultaneously serving as a reservoir for chemical pollutants, generating delayed secondary atmospheric emissions through volatilization that prolong the hazard zone beyond the active release period. Third, ambient wind conditions exert a dominant influence on the directionality, extent, and intensity of the atmospheric hazard zone, underscoring the importance of site-specific meteorological conditions in risk assessment. These findings collectively provide a valuable experimental database for the validation of multiphase dispersion models and the development of improved safety protocols for hazardous liquid and gas release scenarios in marine environments.

4. References

[1] Aprin, L., Cotte, L., Le Bihan, T., Le Floch, S. (2024). Report D2.4 - Experimental study on gas cloud (fire & explosion) - WP2: Enhancing knowledge and data on gases and evaporators, MANIFEST Genius project, Grant Agreement number 101140390.

[2] Wikipedia contributors. (2026, March 9). Ammonia. In Wikipedia, The Free Encyclopedia. Retrieved 13:58, March 14, 2026, from https://en.wikipedia.org/w/index.php?title=Ammonia&oldid=1342489883

[3] CEDRE. (2006). Ammonia Chemical Response Guide.

[4] Adda-Bedia, M., Kumar, S., Lechenault, F., Moulinet, S., Schillaci, M., Vella, D. (2016). Inverse Leidenfrost Effect: Levitating Drops on Liquid Nitrogen. Langmuir 2016 32 (17), 4179-4188. DOI: 10.1021/acs.langmuir.6b00574.

[5] Schremb, M., Kalter, M., Vanapalli, S. (2023). A nitrogen Leidenfrost droplet on a water pool: Experiments, theory and simulations of droplet shrinkage and ice formation, International Journal of Heat and Mass Transfer, Volume 217, 124658, ISSN 0017-9310, https://doi.org/10.1016/j.ijheatmasstransfer.2023.124658.

Co-funded by
the European Union